

# Statistical Study of Medium-Scale Traveling Ionospheric Disturbances in Low-Latitude Ionosphere Using an Automatic Algorithm

**PinHsuan Cheng**

National Cheng Kung University <https://orcid.org/0000-0002-2658-4898>

**Charles Lin** (✉ [charles@mail.ncku.edu.tw](mailto:charles@mail.ncku.edu.tw))

National Cheng Kung University No.1 <https://orcid.org/0000-0001-8955-8753>

**Yuichi Otsuka**

Nagoya University

**Hanli Liu**

High altitude observatory

**Panthalingal Krishanunni Rajesh**

National Cheng Kung University

**Chia-Hung Chen**

National Cheng Kung University

**Jia-Ting Lin**

National Cheng Kung University

---

**Full paper**

**Keywords:** low-latitude MSTIDs, Support Vector Machine, Atmospheric Gravity Waves, Sporadic E layers

**Posted Date:** December 30th, 2020

**DOI:** <https://doi.org/10.21203/rs.3.rs-136037/v1>

**License:** © ⓘ This work is licensed under a Creative Commons Attribution 4.0 International License.

[Read Full License](#)

---

1 **Title: Statistical Study of Medium-Scale Traveling Ionospheric Disturbances in**  
2 **Low-Latitude Ionosphere Using an Automatic Algorithm**

3 Author #1: Pin-Hsuan Cheng, National Cheng Kung University No.1, University  
4 Road, Tainan City 701, Taiwan (R.O.C), p851102peter5@gmail.com

5 Author #2: Charles Chien-Hung Lin, National Cheng Kung University No.1,  
6 University Road, Tainan City 701, Taiwan (R.O.C), charles@mail.ncku.edu.tw

7 Author #3: Yuichi Otsuka, Institute for Space-Earth Environmental Research, Nagoya  
8 University Furo-cho, Chikusa-ku, Nagoya 464-8601, Japan, otsuka@isee.nagoya-  
9 u.ac.jp

10 Author #4: Hanli Liu, 1850 Table Mesa Dr, Boulder, CO USA 80305, liuh@ucar.edu

11 Author #5 Panthalingal Krishanunni Rajesh, National Cheng Kung University No.1,  
12 University Road, Tainan City 701, Taiwan (R.O.C), pkrger@gmail.com

13 Author #6: Chia-Hung Chen, National Cheng Kung University No.1, University  
14 Road, Tainan City 701, Taiwan (R.O.C), koichi@mail.ncku.edu.tw

15 Author #7: Jia-Ting Lin, National Cheng Kung University No.1, University Road,  
16 Tainan City 701, Taiwan (R.O.C), familyiscute@gmail.com

17 **Indicate the corresponding author:**

18 Charles Lin

19

## 20 Abstract

21 This study investigates the medium-scale traveling ionospheric disturbances (MSTIDs)  
22 statistically at the low-latitude equatorial ionization anomaly (EIA) region in the  
23 northern hemisphere. We apply the automatic detection algorithm including the three-  
24 dimensional fast Fourier transform (3-D FFT) and support vector machine (SVM) on  
25 total electron content (TEC) observations, derived from a network of ground-based  
26 global navigation satellite system (GNSS) receivers in Taiwan (14.5°N geomagnetic  
27 latitude; 32.5° inclination), to identify MSTID from other waves or irregularity features.  
28 The obtained results are analyzed statistically to examine the behavior of low-latitude  
29 MSTIDs. Statistical results indicate the following characteristics. First, the southward  
30 (equatorward) MSTIDs are observed almost every day during 0800-2100 LT in Spring  
31 and Winter. At midnight, southward MSTIDs are more discernible in Summer and  
32 majority of them are propagating from Japan to Taiwan. Second, northward (poleward)  
33 MSTIDs are more frequently detected during 1200-2100 LT in Spring and Summer with  
34 the secondary peak of occurrence between day of year (DOY) 100-140. The  
35 characteristics of the MSTIDs are interpreted with additional observations from radio  
36 occultation (RO) soundings of FORMOSAT-3/COSMIC as well as modeled  
37 atmospheric waves from the high-resolution Whole Atmosphere Community Climate

38 Model (WACCM) suggesting that the nighttime MSTIDs in Summer is likely connected  
39 to the atmospheric gravity waves (AGWs).

40 **Keywords:** low-latitude MSTIDs, Support Vector Machine, Atmospheric Gravity  
41 Waves, Sporadic E layers

42

## 43 1.Introduction

44 Traveling ionospheric disturbances (TIDs) are known as the manifestation of  
45 atmospheric gravity waves (AGWs) of lower atmospheric origins (Hines, 1960) in the  
46 ionosphere. Among the TIDs, the disturbances with horizontal wavelength of 100-300  
47 km and phase velocity of 50-300 m/s are classified as medium-scale TIDs (MSTIDs)  
48 (e.g. Hunsucker et al., 1982; Otsuka et al., 2013). MSTIDs were previously studied  
49 using various techniques in the middle latitudes such as all-sky airglow imagers,  
50 ionosondes, incoherent scatter radar, and total electron content (TEC) observations  
51 derived from ground-based global navigation satellite system (GNSS) receivers. (e.g.,  
52 Bowman, 1985, 1989; Garcia et al., 2000; Saito et al., 2002; Shiokawa et al., 2003a,  
53 2006; Otsuka et al., 2004, 2011; Amorim et al., 2011; Medvedev et al., 2017; Takeo et  
54 al., 2017).

55 MSTIDs were previously categorized into daytime and nighttime types according  
56 to their wave characteristics. The daytime MSTIDs at mid-latitude region in northern

57 hemisphere have feature of frontal alignment in east-west (E-W) direction propagating  
58 in meridional north-south (N-S) direction or frontal alignment of southwest-northeast  
59 (SW-NE) direction propagating in northwest-southeast (NW-SE) direction (Hernandez-  
60 Pajares et al., 2012; Kotake et al., 2006; Otsuka et al., 2011). On the other hand, the  
61 nighttime MSTID has a unique frontal alignment in the northwest-southeast (NW-SE)  
62 direction with propagation direction in equator westward direction (Behnke et al., 1979;  
63 Saito et al., 1998; Garcia et al., 2000; Shiokawa et al., 2003a; Kotake et al., 2006;  
64 Tsugawa et al., 2007a; Kubota et al., 2011; Hernández-Pajares et al., 2012; Rajesh et  
65 al., 2016). It is due to such a special frontal alignment, the phenomenon was originally  
66 explained by Perkins instability (*c.f.* Perkins et al., 1973, Behnke, 1979, Garcia et al.,  
67 2000).

68 As the growth rate of Perkins instability is much slower than the observations,  
69 previous studies suggested that the instability also requires seeding perturbation to  
70 induce the instability development. Kelley and Fukao (1991) recommended that AGWs  
71 could be a seeding mechanism to accelerate the Perkins instability. Huang et al. (1994)  
72 suggested that AGWs play an important role in formation of the nighttime MSTIDs due  
73 to the electrodynamic coupling, which was supported by follow-up observations (Miller  
74 et al., 1997; Nicolls and Kelley, 2005). Meanwhile, Shiokawa et al. (2003b) calculated  
75 the theoretical predicted growth of the Perkins instability. The result indicated that the

76 Perkins instability has low growth rate alone and it takes more than 2 hours, which is  
77 much longer than the observations. Recently, Chou et al. (2017, 2018), employed dense  
78 GNSS observations and simulations on the study of MSTIDs driven by typhoon and  
79 proposed that the severe weather driven concentric GWs (CGWs) could accelerate the  
80 Perkins instability by providing additional polarization electric field perturbations  
81 driven by the perturbation winds of CGWs.

82         Additionally, Sporadic E layer (EsL) instability is proposed as an important  
83 indirect driver of the nighttime MSTIDs (Cosgrove and Tsunoda, 2004), which is  
84 mainly produced by the effect of vertical wind shear in E region (Whitehead, 1961;  
85 Mathews, 1998; Carrasco et al., 2007; Haldoupis, 2011; Yeh et al., 2013). EsL  
86 instability can act as a vital character for accelerating growth of Perkins instability by  
87 projecting the polarization electric field perturbations to the F-region. Tsunoda (2006)  
88 showed the analytic results on the acceleration of the instability and Yokoyama et al.  
89 (2009) showed the self-consistent coupling of EsL and F layer Perkins instabilities  
90 through numerical simulations. Both studies have indicated the importance of this E  
91 and F layer coupling for growth of the MSTIDs.

92         Not only occurring at mid-latitude, observational studies also depicted  
93 characteristics of MSTIDs over the low-latitude regions (*c.f.* Shiokawa et al., 2006; Lee  
94 et al., 2008; MacDougall et al., 2011; Fukushima et al., 2012; Narayanan et al., 2014;

95 Jonah et al., 2016; Paulino et al., 2016; Figueiredo et al., 2018). For instance, the  
96 investigations using OI 630.0 nm airglow images taken by all-sky imager around the  
97 transition region of low to mid-latitudes ( $19.3^{\circ}\text{N}$  dip latitude) reported by Narayanan et  
98 al. (2014) suggested that the MSTID could be inhibited by the equatorial ionospheric  
99 anomaly. Shiokawa et al. (2006) and Fukushima et al. (2012) suggested that the  
100 directionalities of MSTIDs over Kototabang ( $10.4^{\circ}\text{S}$  dip latitude) are different from the  
101 typical MSTIDs observed at the mid-latitudes and attribute their formation by gravity  
102 waves. Paulino et al. (2016) carried out an investigation at the off-equatorial region,  
103 over São João do Cariri, by using airglow observations over nearly a solar cycle and  
104 speculated that the gravity waves are the likely source of the periodic MSTIDs.

105 As described above, MSTIDs were statistically studied in the ionosphere for quite  
106 a long time in mid-latitude region with some additional documentations over low-  
107 latitude region possibly driven by various physical mechanisms. Most of the studies,  
108 however, were performed mainly by adopting visual inspection of the observation data  
109 that requires time consuming efforts and could be influenced by subjective bias while  
110 inspecting the airglow images or TEC maps. Takeo et al. (2017) performed three-  
111 dimensional fast Fourier transform (3-D FFT) to detect the MSTIDs automatically in  
112 airglow imagers over a solar cycle for the first time. Here, our main goal is to develop  
113 an autonomous detection algorithm by combining the 3-D FFT and support vector

114 machine (SVM) to distinguish and categorize MSTIDs from other waves or  
115 irregularities in the GNSS-TEC maps.

116 In this study, the autonomously identified MSTIDs at low to mid-latitudes are  
117 statistically organized according to their wave parameters, i.e. wavelength, amplitude,  
118 propagation direction, seasonal and local time (LT) dependences. The possible  
119 mechanisms responsible for these low-latitude MSTIDs are discussed based on these  
120 statistical results with aids from the EsL observation obtained from the radio occultation  
121 (RO) observations of FORMOSAT-3/COSMIC (Yeh et al., 2014) and the AGWs  
122 simulated by the high-resolution Whole Atmosphere Community Climate Model  
123 (WACCM) (Liu et al., 2014).

124

## 125 2.Methodology

126 We develop an autonomous algorithm to detect MSTIDs by using both the 3-D  
127 FFT and the SVM. As the equatorial plasma bubbles (EPBs) affected by zonal neutral  
128 winds could appear in the reverse C-shape spatial distribution (Shiokawa et al. 2004;  
129 Kil et al., 2009) showing NW-SE (NE-SW) waveform in the northern (southern)  
130 hemisphere similar to the frontal alignment of MSTIDs, it is important to have the  
131 algorithm capable of distinguishing the two different instabilities. The algorithm is  
132 applied on the GNSS data around Taiwan (20-30°N, 115-125°E geographic

133 latitude/longitude and 15°N dip latitude) under the northern EIA crest during 2013-  
134 2015 to study the characteristics, e.g. propagation direction, LT and seasonal  
135 dependence, of MSTIDs and EPBs.

136 Before carrying out the 3-D FFT and SVM, a 60 mins. high pass filter is applied  
137 to the GNSS-TEC data followed by interpolation of the filtered TECs into the fixed  
138 grids with spatial resolution of ~0.5 deg. latitude/longitude in both zonal and meridional  
139 direction with an accumulation period of 30 mins. It should be noted that we substitute  
140 zero to the region with no available data owing to the limited coverage of GNSS  
141 observation around Taiwan. The ionospheric pierce point (IPP) for converting slant to  
142 vertical TEC is set at 300 km altitude. Figure 1a shows an example of the filtered TEC  
143 over the region and Figure 1b illustrates the grids for the autonomous detection  
144 algorithm.

145 We exploit the 3-D FFT method similar to that developed by Matsuda et al. (2014)  
146 to the cumulative three-dimensional filtered TEC data for the zonal and meridional  
147 wave numbers and angular frequency. It is noted that positive wave number represents  
148 northward or eastward direction of propagation. The phase velocities ( $V_p$ ) of the waves  
149 are given in terms of the parameters obtained from the 3-D FFT as follows,

150

151 
$$V_p = \sqrt{\left(\frac{\omega}{2\pi} \frac{W_m}{K}\right)^2 + \left(\frac{\omega}{2\pi} \frac{W_z}{L}\right)^2} \quad (1)$$

152

153 where  $W_m$  and  $W_z$  are meridional and zonal width of the detection region;  $K$ ,  $L$  and  $\omega$   
154 represent meridional wave numbers, zonal wave numbers and angular frequency,  
155 respectively. The propagation direction ( $\theta$ ) is given as,

156

$$157 \quad \theta = \varnothing + \tan^{-1} \frac{\left(\frac{W_m}{L}\right)^2}{\left(\frac{W_z}{K}\right)^2} \quad (2)$$

158

159 where  $\varnothing$  is the azimuth angle, which depends on the value of both zonal and  
160 meridional wave numbers.

161 The 3-D FFT will provide a weaker artificial enhancement of power spectral  
162 density (PSD) in the opposite direction than that of the true direction (Takeo et al., 2017).  
163 Therefore, the maximum PSD is taken to determine the direction for each computation  
164 to rule out the wrong directions in this study.

165 From the computed results together with the TEC observations, we obtain 10 kinds  
166 of parameters including horizontal wavelength, meridional and zonal wave numbers,  
167 phase velocity, propagation direction, angular frequency, PSD of the 3-D FFT,  
168 minimum TEC, day of year (DOY) and universal time (UT). These parameters are  
169 exploited for training the SVM model in order to distinguish MSTID, EPB and quiet  
170 time background ionosphere. The detailed procedures for creating the SVM model is

171 illustrated in Figure 2. In the SVM model, we create a ten-dimensional space where the  
172 coordinates stem from the 10 kinds of parameters mentioned above. The data are  
173 represented as points and are mapped into the 10-dimensional (10-D) space according  
174 to the corresponding values of each parameter. In the 10-D space, the SVM model  
175 separates different classes by computing the best boundaries called hyperplanes. New  
176 data are then mapped into that same space and are predicted into various classes based  
177 on the side of the hyperplane on which they might fall. Presumably, the hyperplane  
178 between anisotropy classes should be as wide as it could be to maintain the quality of  
179 the SVM model. Therefore, a soft-margin method, defining the width of a hyperplane  
180 in non-linear classification, is applied on supporting the hyperplane. We define a  
181 hyperplane with a soft-margin in the following form (Chen et al., 2004; Chang et al,  
182 2011),

183

$$184 \quad |N_h \cdot x - b| \geq 1 \pm \varepsilon_i \quad (3)$$

185

186 where  $N_h$  represents the normal vector to the hyperplane;  $x$  refers to the normalized  
187 10-D parameters;  $b$  is a normal constant; the normal constant (on the right-hand side of  
188 the equation) "1" or "-1", considering the absolute value, indicates two different classes;  
189  $\varepsilon_i$  represents slack variable which determine the width of the soft-margin. It should be

190 apparent that the greater the value of slack variable is, the larger the breadth of the soft-  
191 margin would be. In order to maintain the quality of classification, the slack variable  
192 should as small as it could be where we set the value as 0.4 in our case.

193 In this study, a supervised learning method is used for classifying the different  
194 classes. Supervised learning indicates that we have to label the classes for the raw data  
195 to create input-output pairs before training the SVM model. In our case, we label the  
196 different classes using discriminants and a little visual inspection for validation. During  
197 the training processes, a solar maximum year, 2000, and a solar minimum year, 2009,  
198 are used for training and testing the model quality since MSTIDs and EPBs have a  
199 different solar activity dependence. Due to the 30 mins time resolution in the 3D-FFT  
200 computation, the total number of data for these two years are around 35000. The dataset  
201 is randomly separated into two groups including 80% of training data (~28000 piece)  
202 and the other 20% of testing data (~7000 piece). The training data are used for training  
203 the model by computing a hyperplane for categorizing anisotropy classes. On the other  
204 hand, the testing data applied on testing the trained model are utilized for calculating  
205 the accuracy rate of the SVM model prediction. Here, the accuracy is the ratio of  
206 number of correct predictions to the total number of input samples. During the testing  
207 processes, the dataset is repeatedly split into training data and testing data for five times

208 to test the model performance. The testing results indicate that our model has over 96%  
209 accuracy rate for distinguishing MSTID, EPB and ionosphere without irregularity.

210

### 211 3.Results and Discussions

212 In the analysis, we define the four seasons as follows: (1) Spring: from 6 February  
213 to 6 May for 3 months, centering on the spring equinox; (2) Summer: from 6 May to 6  
214 August for 3 months, centering on the summer solstice; (3) Fall: from 6 August to 6  
215 November for 3 months, centering on the fall equinox; and (4) Winter: from 6  
216 November to 6 February for 3 months, centering on the winter solstice.

217 Since the EPB is a well-known phenomenon in the low-latitude ionosphere which  
218 was investigated intensively, it is conceivable to validate the characteristics of EPBs,  
219 using our algorithm, such as occurrence rate, propagation direction and seasonal  
220 dependence. Here, the occurrence rate is defined as the ratio between the number of  
221 events in which EPBs are observed ( $M$ ) and the amount of data in which GNSS-TEC  
222 exist ( $N$ ). Since the GNSS-TEC data are available every 30 seconds during 2013-2015,  
223 the value of  $N$  is identical in each occurrence rate computation.

224 The observed characteristics of EPBs during 2013-2015 can be summarized as  
225 follows (figure not shown). First, the EPBs are usually observed at the LT period of  
226 2000-0200 with an eastward propagation direction. Second, the occurrence rate of EPBs

227 is higher in the solar maximum year of 2014, showing the dependence on the solar  
228 activity. Third, the cumulative occurrence rate for these years indicates that the seasonal  
229 occurrence rate of EPBs is descending in the order from Spring, Fall, Summer, to Winter.  
230 The characteristics of EPBs in their diurnal and seasonal variations are consistent with  
231 those reported in the previous studies (e.g. Sahai et al., 2000; Huang et al., 2002;  
232 Pimenta et al., 2003; Fejer et al., 2005; Gentile et al., 2006; Yao & Makela, 2007;  
233 Paulino et al., 2011; Sharma et al., 2014; Sun. et al., 2016) suggesting the reliability of  
234 our algorithm.

235

### 236 3.1 Observation Results

237 In this section, we display the annual variations (2013-2015) of the characteristics  
238 of MSTIDs by excluding the possible contamination coming from EPBs. The  
239 wavelength and horizontal phase velocity characteristic of MSTIDs over Taiwan are  
240 respectively among 100-400 km and 100-250 m/s which are consistent with the  
241 previous studies (e.g. Hunsucker et al., 1982; Otsuka et al., 2013). The occurrence rate  
242 of MSTIDs are calculated by using the same approach applied for calculation of the  
243 occurrence of EPBs described in Section 3. The results illustrate that the occurrence  
244 and propagation characteristics of MSTIDs have clear seasonal and LT dependences.  
245 The occurrence rate of southward MSTIDs (Figure 3a-c) indicates that they are more

246 discernable during 0800-2100 LT in Spring and Winter. During Summer, southward  
247 MSTIDs mainly occur around 2100-0300 LT. On the contrary, the occurrence rate of  
248 northward MSTIDs (Figure 3d-3f) demonstrates that they are more frequently observed  
249 around 1200-2100 LT from Spring to Fall with a secondary peak occurring around  
250 0000-0300 LT between DOY 100-140. In Figure 3g-3i, a transition boundary between  
251 the northward and southwestward MSTIDs takes place three hours after sunset at  
252 around 2100 LT during Summer. It is noteworthy that the LT dependence of the  
253 southwestward MSTIDs takes place much later after sunset than those reported in the  
254 previous literatures (Behnke et al., 1979; Saito et al., 1998; Garcia et al., 2000;  
255 Shiokawa et al., 2003a; Kotake et al., 2006; Tsugawa et al., 2007a; Kubota et al., 2011;  
256 Hernández-Pajares et al., 2012; Otsuka et al., 2013), which suggests an alternative  
257 driving mechanism should be proposed. A rational explanation is that the  
258 southwestward MSTIDs are mainly propagating from higher latitude to the lower  
259 latitude over Taiwan region instead of being generated locally.

260       The filtered TEC over Japan and Taiwan (Figure 4a-4b) reveals the relationship  
261 between the MSTIDs at low and mid latitudes. To identify the characteristics of the  
262 MSTIDs over Japan and Taiwan, we organize filtered TEC as a function of distances  
263 and time (Figure 4c). The filtered TEC along the orange dash line in Figure 4b is chosen  
264 for organizing Figure 4c for studying the characteristics of MSTIDs in this case. The

265 daytime MSTIDs (Figure 4a) propagate toward southeast and northwest over Japan and  
266 Taiwan, respectively. On the contrary, the nighttime MSTIDs (Figure 4b) demonstrate  
267 that they are propagating southwestward over Japan and across a long distance to reach  
268 Taiwan region. In Figure 4c, results apparently show that the MSTIDs over Japan have  
269 greater wave amplitudes ( $\sim 0.2$  TECu, where  $1 \text{ TECu} = 10^{16} \text{ el/m}^2$ ) and longer  
270 wavelengths ( $\sim 250$  km) than those over Taiwan where the wave amplitude is around  
271  $0.1$  TECu and the wavelength is about  $100$  km. The red rectangle in Figure 4c, therefore,  
272 illustrates that the MSTIDs around  $1400$ - $2100$  UT ( $2200$ - $0500$  LT) over  $22$ - $28^\circ\text{N}$   
273 latitude are mainly coming from Japan as they have a greater TEC amplitude fluctuation  
274 and wavelengths than those in the same latitudes at earlier local times.

275 To further identify the relationship between the MSTIDs over Japan and Taiwan,  
276 we compare the propagation direction with normalized power spectral density (PSD) of  
277 MSTIDs (Figure 5) between DOY  $100$ - $300$  during  $2013$ - $2015$ . The PSD derived from  
278 3-D FFT indicates the power of the waves, which corresponds to the square of the  
279 amplitude fluctuation. The normalized PSD with greater value, indicating perturbations  
280 with greater wave amplitude, mainly occur three hours after sunset. This is in good  
281 agreement with the southwestward MSTID observations, further suggesting that these  
282 MSTIDs are mainly propagating from Japan instead of being generated over Taiwan.

283

## 284 3.2 Perkins /Es Layer Instability and MSTIDs

285 For the nighttime MSTIDs, Perkins instability (Perkins, 1973) was considered as  
286 the most plausible generation mechanism to explain the special wavefront alignment  
287 (NW-SE) of MSTIDs (Benke, 1979; Garcia et al., 2000). According to Shiokawa et al.  
288 (2003) and Tsunoda (2006), the linear growth rate ( $\gamma_p$ ) of the Perkins instability can be  
289 given as:

290

$$\begin{aligned} 291 \quad \gamma_p &= \frac{g}{H_n \langle v_{in} \rangle} \frac{\sin^2(I) \sin(\theta - \alpha) \sin(\alpha)}{\cos(\theta)} \\ 292 \quad &= \frac{E_0 \sin(\theta - \alpha) \sin(\alpha) \cos(I) \langle v_{in} \rangle_{ot}}{BH_n \langle v_{in} \rangle} \end{aligned} \quad (4)$$

294

295 where  $g$ ,  $H_n$  and  $v_{in}$  are the gravitational acceleration, scale height of neutral  
296 atmosphere and ion-neutral collision frequency;  $I$  represents the magnetic inclination;  
297  $\theta$  is the angle of background electric field from east;  $\alpha$  means the angle between the  
298 direction normal to the frontal structure and east;  $E_0$ ,  $B$  and are the background electric  
299 field and magnetic field; subscript  $0t$  represents inclusion of a tangential component.

300 Notice that  $\alpha$  should greater than zero but less than or equal to  $\theta$ .

301 In Equation (4), the ion-neutral collision frequency is inversely proportional to the  
302 growth rate. The neutral density is small during solstices and magnetically quiet periods

303 of solar activity, which generates a lower ion-neutral collision frequency. This effect  
304 could produce a high occurrence rate of nighttime MSTIDs during solstices and low  
305 solar flux years which agree with the previous literatures (e.g. Shiokawa et al., 2003a;  
306 Kotake et al., 2006).

307 On the other hand, a coupled electrodynamical system between EsL and F region  
308 also plays an important role to accelerate the growth rate for nighttime MSTIDs (e.g.  
309 Cosgrove & Tsunoda, 2004; Tsunoda, 2006; Yokoyama et al., 2009). In this study, we  
310 estimate the occurrence of EsL by using FORMOSAT-3/COSMIC (F3/C) radio  
311 occultation (RO) data for comparing with the MSTIDs characteristics in nighttime  
312 during 2013-2015. Resende et al. (2018) revealed that the S4 scintillation index derived  
313 from the F3/C RO profiles, which provide the disturbance information from the signal  
314 to noise ratio (SNR) of the electron density from GPS L1 band, is suitable to estimate  
315 the EsL at low latitudes due to their high correlation. In this case, an S4 threshold of 0.3  
316 is set over 80-130 km altitudes (*c.f.* Whitehead, 1989; Chu et al., 2014; Yeh et al., 2014;  
317 Tsai et al., 2018) for evaluating the occurrence of EsL. It is noteworthy that the EsL do  
318 not have a conjugate effect but the MSTIDs are presented as conjugate structures in  
319 both hemispheres according to previous studies (Saito et al., 1998; Otsuka et al., 2004;  
320 Martinis et al., 2019). That is, the EsL occurring at one of the hemispheres could trigger  
321 the MSTID in both hemispheres, coherently. As a result, two detection regions are

322 formed, which are (i) Taiwan region, the same as mentioned in Section 2, and (ii) the  
323 conjugate region of Taiwan, the identical meridional and zonal breadth to (i) but  
324 centering at 120°E geomagnetic longitude; -4°S geomagnetic latitude, for investigating  
325 the EsL characteristics in nighttime during 2013-2015.

326 The EsL mainly occur in Summer but the occurrence is much less over Taiwan  
327 (Figure 6a) than over Japan (Otsuka et al., 2008) in nighttime, which is consistent with  
328 the previous study (Zhou et al., 2017). On the contrary, the southward/northward  
329 (Figure 6c/6d) MSTIDs still have considerable occurrence rate until 2200 LT in Spring  
330 and Winter/2100 LT in Spring to Fall with the identical propagation direction (Figure  
331 6b) before and after the dusk terminator (black line). Also, the propagation direction of  
332 the northward MSTIDs (Figure 7) illustrates that the MSTIDs mainly propagate  
333 northwestward (wavefront of NE-SW direction) and exactly northward (wavefront of  
334 E-W direction), which are inconsistent with the theoretical wavefront alignment (NW-  
335 SE) of Perkins instability and EsL instability (Perkins, 1973; Cosgrove and Tsunoda,  
336 2004). The anisotropy characteristics between EsL and MSTIDs rules out the possibility  
337 that the Perkins instability and EsL instability are responsible for generating the  
338 nighttime MSTIDs over Taiwan.

339

### 340 3.3 Gravity Waves and MSTIDs

341 As the characteristics of EsL (Perkins instability) do not favor MSTIDs generation  
342 and propagation, AGWs are considered as a plausible driver of the northward-  
343 propagating MSTIDs in Spring and Summer nighttime over Taiwan. The secondary  
344 peak of occurrence of northward MSTIDs taking place post-midnight between DOY  
345 100-140 should be amenable to interpretation in terms of AGWs. Figure 8 displays an  
346 example of 557 nm airglow images on 29 April 2020 around 0209-0239 LT, obtained  
347 from an all sky imager operating at Tainan Astronomical Education Area (120.39°E;  
348 23.18°N). The images, mainly contributed from about 95-97 km altitude, are used to  
349 evaluate the horizontal structures of AGWs during this period. Using the 3-D FFT, the  
350 series of airglow images demonstrate the salient northeastward propagation of AGWs  
351 with a horizontal phase velocity, horizontal wavelength, and period of ~114 m/s, ~83  
352 km, and ~12 min. respectively over Taiwan. Meanwhile, the filtered TEC map with an  
353 IPP at 300 km altitude (Figure 9) reveals the northeastward MSTIDs with a horizontal  
354 phase velocity, horizontal wavelength, and period of ~147 m/s, ~151 km, and ~17 min.,  
355 respectively. The nearly identical propagation direction and similar characteristics of  
356 AGWs and MSTIDs suggesting that AGWs should be responsible for the nighttime  
357 MSTIDs over Taiwan for this event. However, the time characteristic in the airglow  
358 images and filtered TEC maps are different in this case suggesting that further  
359 correlation between each other should be proposed.

360 To further understand the correlation between AGWs and MSTIDs, we evaluate  
361 the resolved AGWs derived from high-resolution WACCM among 30 June to 11 July.  
362 In the high resolution WACCM, the horizontal and vertical resolution are  $\sim 0.25^\circ$  and  
363  $\sim 700$  m, respectively. In this case, we investigate AGWs horizontal structure at 5.8e-  
364 4hpa ( $\sim 93$  km) altitude (*c.f.* Zhou et al., 2002; Suzuki et al., 2007; Chun and Kim, 2008;  
365 Heale et al., 2020) in the WACCM. Taking 1400 UT on 9 July for example, the zonal  
366 wind (Figure 10a) and meridional wind (Figure 10b) patterns display several salient  
367 northwestward AGWs structures propagating over north Pacific Ocean and across a  
368 long distance  $\sim 2800$  km along the Philippines, before reaching Taiwan. In this case, the  
369 waves structures mostly dissipate around  $30^\circ\text{N}$  geographic latitude by the stronger in  
370 phase background wind. In Figure 10c-10d, we estimate the morphological  
371 characteristics of AGWs as a function of time and distances by organizing the zonal and  
372 meridional wind along the yellow arrow in Figure 10a and 10b. Several long-lasting,  
373  $\sim 12$  hr, northwestward AGWs are found during this period with a horizontal wavelength  
374 of tens to hundreds of km and a horizontal phase velocity among 20-85 m/s which are  
375 consistent with previous literatures (Piani et al., 2000; Horinouchi et al., 2002; Sentman  
376 et al., 2003; Suzuki et al., 2007; Takeo et al., 2017; Tsuchiya et al., 2019).

377 In Figure 11, the propagation direction characteristic of AGWs (red line with stars),  
378 obtained from the 3-D FFT over Taiwan, is compared to the MSTID observations (blue

379 line) in Summer during 2013-2015. The locally generated MSTIDs mainly occurring  
380 during 1200-2100 LT in Summer (Figure 3) are in good agreement with the  
381 corresponding WACCM output suggesting that AGWs may play a role in the generation  
382 of MSTIDs during this period. However, there is a clear disagreement occurring after  
383 2000 LT showing southwestward propagation of MSTIDs while AGWs are northward.  
384 The disagreement confirms that the southwestward MSTIDs after 2100 LT mainly come  
385 from the southwestward propagation of MSTIDs originated from Japan as described in  
386 Section 3.1.

387 Tsugawa et al (2007a) suggested that the MSTID activity over Japan is highest in  
388 the nighttime during 2100-0300 JST in Summer (May-August or DOY 140-250). Since  
389 the amplitude of the MSTIDs over Japan is greater than that over Taiwan, it is difficult  
390 to isolate any influence of Japan MSTID's in the overlapping TEC observations over  
391 Taiwan. However, the DOY from 100-140, when the southwestward MSTIDs over  
392 Japan were least observed could be the opportunity for the identification of locally  
393 generated MSTIDs over Taiwan. This characteristic of MSTIDs, when they are present,  
394 is consistent with a secondary occurrence peak of the northward MSTIDs over Taiwan  
395 suggesting that this secondary peak of northward MSTIDs could be identified owing to  
396 the least occurrence of MSTIDs over Japan during the period. Also, the propagation  
397 direction characteristic of AGWs after 2000 LT (Figure 11) is mainly propagating

398 northwestward which is consistent with the secondary peak of the MSTIDs  
399 observations (Figure 7). It suggests that AGWs is likely an important seeding driver for  
400 generation of the northward-propagating MSTIDs over Taiwan in nighttime in Summer.  
401 Based on the propagation directions and seasonal occurrences, we suggest that the  
402 AGWs have a great contribution to the low latitude MSTIDs in both daytime and  
403 nighttime in Summer.

404

#### 405 4. Discussion

406       Regarding the southwestward MSTIDs taking place ~3 hours after sunset, an  
407 alternative explanation is that they are mainly coming from mid-latitude region. AGWs  
408 seeding, however, could be a plausible mechanism to accelerate the Perkins instability  
409 where the growth of the instability could be significantly enhanced and accelerated  
410 (Kelly and Fukao, 1991; Huang et al., 1994; Chou et al., 2017). Such a mechanism,  
411 hence, indicates that the southwestward MSTIDs could be generated locally due to the  
412 Perkins instability as well. In order to understand further about the generation  
413 mechanism of the southwestward MSTIDs, the occurrence rate of southwestward  
414 MSTIDs are compared between Japan and Taiwan. Otsuka et al. (2011) revealed that  
415 the occurrence rate is ~30% over Japan in a solar maximum year in nighttime in  
416 Summer. Our study, however, shows the higher occurrence rates of ~40% in a solar

417 maximum year. It should be apparent that the MSTIDs should be generated locally since  
418 the higher occurrence rates over Taiwan is inconsistent with the hypothesis that the  
419 southwestward MSTIDs mainly come from Japan. However, the solar activity condition  
420 in our study (f10.7 index is 145.9 s.f.u.) is much weaker than that proposed by Otsuka  
421 et al. (2011) (f10.7 index is 179.4 s.f.u.) suggesting that the further relationship between  
422 the MSTIDs over Japan and Taiwan should be investigated in the future works.

423

## 424 5.Summary

425 In this study, we utilize both the 3-D FFT and SVM to statistically investigate the  
426 MSTIDs in the low latitude equatorial ionization anomaly region over Taiwan during  
427 2013-2015. As EPBs have some characteristics similar to MSTIDs, the occurrence of  
428 EPBs is also investigated in order to distinguish it from the MSTIDs. Several important  
429 features such as the variation of the propagation direction and occurrence rates are  
430 revealed in this study. The main findings are summarized as follows.

431

- 432 1. The statistical results show that the seasonal, LT variations and solar activity  
433 dependence are generally consistent to previous studies of MSTIDs and EPBs,  
434 indicating that our algorithms could successfully distinguish EPBs and MSTIDs  
435 in the TEC perturbations.

436 2. The occurrence rate and propagation direction of MSTIDs have clear seasonal  
437 and LT dependences. In Spring and Winter, southward MSTIDs are observed  
438 almost every day during 0800-2100 LT, and in Summer they appear mainly  
439 during 2100-0300 LT and have least occurrence in Autumn. On the contrary,  
440 northward MSTIDs are observed more frequently during 1200-2100 LT from  
441 Spring to Autumn with a secondary peak during 0000-0300 LT between DOY  
442 100-140.

443 3. The propagation directions of MSTIDs patterns display a clear boundary for  
444 northward and southwestward MSTIDs at 2100 LT in Summer. During 1200-  
445 2100 LT, the MSTIDs mainly propagate northward and northwestward. On the  
446 other hand, the MSTIDs observed during 2100-0300 LT mainly propagating  
447 southwestward are majorly coming from Japan, mid-latitude region.

448 4. By comparing the occurrence of MSTIDs over Japan and Taiwan, we suggest  
449 that the MSTID in Taiwan region are influenced by the southwestward-  
450 propagating MSTIDs from Japan during 2100-0300 LT between DOY 140-250  
451 due to the overlapping in TEC observations. A secondary occurrence peak of  
452 northward MSTIDs during 0000-0300 LT between DOY 100-140, therefore,  
453 could be generated owing to the least occurrence of MSTIDs over Japan.

454 5. The wavefront alignment characteristic of nighttime MSTIDs is inconsistent  
455 with the Perkins and EsL instability, ruling out the possibility of these generation  
456 mechanisms. In contrast, the relationship between  $\lambda 557\text{nm}$  airglow images and  
457 filtered TEC map together with a simulation result from WACCM illustrate that  
458 MSTIDs over Taiwan are likely generated by AGWs during both daytime and  
459 nighttime in Summer due to the similar characteristics between MSTIDs and  
460 AGWs.

461

## 462 **Declarations**

### 463 **Ethics approval and consent to participate**

464 Not applicable.

### 465 **Consent for publication**

466 Not applicable.

### 467 **List of abbreviations**

468 AGWs : atmospheric gravity waves.

469 CGWs : concentric gravity waves.

470 DOY : day of year.

471 EIA : equatorial ionization anomaly.

472 EPBs : equatorial plasma bubbles.

- 473 EsL : sporadic E layer.
- 474 F3/C : FORMOSAT-3/COSMIC.
- 475 GNSS : global navigation satellite system.
- 476 IPP : ionospheric pierce point.
- 477 LT : local time.
- 478 MSTIDs : medium-scale traveling ionospheric disturbances.
- 479 PSD : power spectral density.
- 480 RO : radio occultation.
- 481 SNR : signal to noise ratio.
- 482 SVM : support vector machine.
- 483 S4 : scintillation index.
- 484 TEC : total electron content.
- 485 TIDs : traveling ionospheric disturbances.
- 486 UT : universal time.
- 487 WACCM : Whole Atmosphere Community Climate Model.
- 488 3-D FFT : three-dimensional fast Fourier transform.
- 489 **Availability of data and materials**

490 The GNSS-TEC data are provided by the Central Weather Bureau in Taiwan  
491 (<https://gdms.cwb.gov.tw/>) and Geospatial Information Authority in Japan  
492 (<http://www.gsi.go.jp/ENGLISH/index.html>). The F3/C data are provided by  
493 Taiwan Analysis Center for COSMIC (TACC) (<https://tacc.cwb.gov.tw/v2/>). The  
494 all sky imagers data are available on the all sky observatory (ALSO) ([http://allsky-  
495 airglow.earth.ncku.edu.tw/PicWeb/MainHTML/2020/04/29](http://allsky-airglow.earth.ncku.edu.tw/PicWeb/MainHTML/2020/04/29)). The f10.7 index is  
496 derived from OMNIWeb Service under Space Physics Data Facility (SPDF) in  
497 NASA (<https://omniweb.gsfc.nasa.gov/>).

#### 498 **Competing interests**

499 The authors declare that they have no competing interests.

#### 500 **Funding**

501 This paper is supported by Ministry of Science and Technology (MOST) of Taiwan  
502 to National Cheng Kung University under the project MOST 108-2638-M-006-  
503 001-MY2.

#### 504 **Authors' contributions**

505 PHC drafted the manuscript, created the SVM model, carried out 3D-FFT method,  
506 program coding and analyzed the data. CHL and PKR critically evaluated the text  
507 for scientific content and elaborated it. CHL and YO gave very important  
508 conceptions on analyzing the observational results. HLL dealt with the WACCM.

509 PKR and JTL established the airglow images. CHC constructed the TEC filter. All  
510 authors read and approved the final manuscript.

### 511 **Acknowledgements**

512 Thanks to the Central Weather Bureau, Geospatial Information Authority, TACC  
513 and ALSO provide the data. Also, thanks to the MOST supports the funding.

514

### 515 **References**

516 Amorim, D. C. M., Pimenta, A. A., Bittencourt, J. A., & Fagundes, P. R. (2011). Long  
517 term study of medium-scale traveling ionospheric disturbances using oi 630 nm  
518 all sky imaging and ionosonde over Brazilian low latitudes. *Journal of*  
519 *Geophysical Research*, 116, A06312. doi.org/10.1029/2010JA016090

520 Arras, C., J. Wickert, G. Beyerle, S. Heise, T. Schmidt, and C. Jacobi (2008), A global  
521 climatology of ionospheric irregularities derived from GPS radio occultation,  
522 *Geophys. Res. Lett.*, 35, L14809, doi:10.1029/2008GL034158.

523 Arras, C., C. Jacobi, and J. Wickert (2009): Semidiurnal tidal signature in sporadic E  
524 occurrence rates derived from GPS radio occultation measurements at higher  
525 midlatitudes, *Ann. Geophys.*, 27, 2555–2563.

526 Behnke, R. (1979), F layer height bands in the nocturnal ionosphere over Arecibo, J.  
527 *Geophys. Res.*, 84, 974–978, doi:10.1029/JA084iA03p00974.

528 Bowman, G. G. (1985). Some aspects of mid-latitude spread-Es and its relationship  
529 with spread-F. *Planetary and Space Science*, 33(9), 1081–1089.  
530 doi.org/10.1016/0032-0633(85)90027-3

531 Bowman, G. G., Quasi-periodic scintillations at mid-latitudes and their possible  
532 association with ionospheric sporadic-E structures, *Ann. Geophys.*, 7, 259, 1989.

533 Burges, C. J. (1998). A tutorial on support vector machines for pattern recognition. *Data*  
534 *mining and knowledge discovery*, 2(2), 121-167.

535 Carrasco, A. J., I. S. Batista, and M. A. Abdu, Simulation of the sporadic E layer  
536 response to prereversal associated evening vertical electric field enhancement near  
537 dip equator, *J. Geophys. Res.*, 112, A06324, doi:10.10292006JA01243, 2007.

538 C.-C. Chang and C.-J. Lin. LIBSVM: a library for support vector machines, 2001.  
539 Software available at <http://www.csie.ntu.edu.tw/~cjlin/libsvm>.

540 D. R. Chen, Q. Wu, Y. Ying, and D.-X. Zhou, Support vector machine soft margin  
541 classifiers: Error analysis, *J. Mach. Learn. Res.* 5 (2004), 1143–1175.

542 Chou, M. Y., Lin, C. C., Yue, J., Chang, L. C., Tsai, H. F., & Chen, C. H. (2017).  
543 Medium-scale traveling ionospheric disturbances triggered by Super Typhoon  
544 Nepartak (2016). *Geophysical Research Letters*, 44(15), 7569-7577.

545 Chou, M. Y., C. H. Lin, J. D. Huba, Lein, C. P., C. H. Chen, J. Yue, L. C. Chang and P.  
546 K. Rajesh (2018), Numerical modeling of the concentric gravity wave seeding of

547 low-latitude nighttime medium-scale traveling ionospheric disturbances,  
548 Geophysical Research Letters, 45. <https://doi.org/10.1029/2018GL077959>

549 Chun, H. Y., & Kim, Y. H. (2008). Secondary waves generated by breaking of  
550 convective gravity waves in the mesosphere and their influence in the wave  
551 momentum flux. *Journal of Geophysical Research: Atmospheres*, 113(D23).

552 Cooley, J. W., & Tukey, J. W. (1965). An algorithm for the machine calculation of  
553 complex Fourier series. *Mathematics of computation*, 19(90), 297-301.

554 Cosgrove, R. B., and R. T. Tsunoda (2004), Instability of the E-F coupled nighttime  
555 midlatitude ionosphere, *J. Geophys. Res.*, 109, A04305,  
556 doi:10.1029/2003JA010243.

557 Chu, Y. H., Wang, C. Y., Wu, K. H., Chen, K. T., Tzeng, K. J., Su, C. L., ... & Plane, J.  
558 M. C. (2014). Morphology of sporadic E layer retrieved from COSMIC GPS radio  
559 occultation measurements: Wind shear theory examination. *Journal of*  
560 *Geophysical Research: Space Physics*, 119(3), 2117-2136.

561 Danielson, Gordon C.; Lanczos, Cornelius (1942). "Some improvements in practical  
562 Fourier analysis and their application to x-ray scattering from liquids". *Journal of*  
563 *the Franklin Institute*. 233 (4): 365–380.

564 Ding F, Wan W, Xu G, Yu T, Yang G, Wang J (2011) Climatology of medium-scale  
565 traveling ionospheric disturbances observed by a GPS network in Central China.  
566 J Geophys Res 116:A09327. <https://doi.org/10.1029/2011JA016545>

567 Farley, D. T., Bonelli, E., Fejer, B. G., and Larsen, M. F. (1986). The prereversal  
568 enhancement of the zonal electric field in the equatorial ionosphere. J. Geophys.  
569 Res. 91,13,723.

570 Fejer, B. G., Souza, J. R., Santos, A. S., & Costa Pereira, A. E. (2005). Climatology of  
571 F region zonal plasma drifts over Jicamarca. Journal of Geophysical Research, 110,  
572 A12310.

573 Figueiredo, C. A. O. B., Takahashi, H., Wrasse, C. M., Otsuka, Y., Shiokawa, K., &  
574 Barros, D. (2018). Medium-scale traveling ionospheric disturbances observed by  
575 detrended total electron content maps over Brazil. Journal of Geophysical  
576 Research: Space Physics, 123(3), 2215-2227.

577 Fukushima, D., K. Shiokawa, Y. Otsuka, and T. Ogawa (2012), Observation of  
578 equatorial nighttime medium-scale traveling ionospheric disturbances in 630-nm  
579 airglow images over 7 years, J. Geophys. Res., 117, A10324,  
580 doi:10.1029/2012JA017758.

581 Garcia, F. J., M. C. Kelley, J. J. Makela, and C.-S. Huang (2000), Airglow observations  
582 of mesoscale low-velocity traveling ionospheric disturbances at midlatitudes, *J.*  
583 *Geophys. Res.*, 105(A8), 18,407–18,415, doi:10.1029/1999JA000305.

584 Gentile, L. C., Burke, W. J., & Rich, F. J. (2006). A climatology of equatorial plasma  
585 bubbles from DMSP 1989–2004. *Radio Science*, 41(5).

586 Haldoupis C. 2011. A tutorial review on sporadic E layers. In *Aeronomy of the Earth's*  
587 *atmosphere and ionosphere* (eds A Bhattacharyya, MA Abdu, D Pancheva), pp.  
588 381–394. Dordrecht, The Netherlands: Springer.

589 Heale, C., Bossert, K., Vadas, S. L., Hoffmann, L., Dörnbrack, A., Stober, G., Snively,  
590 J. B., & Jacobi, C. (2020). Secondary gravity waves generated by breaking  
591 mountain waves over Europe. *Journal of Geophysical Research: Atmospheres*, 125,  
592 e2019JD031662. <https://doi.org/10.1029/2019JD031662>

593 Hernández-Pajares, M., Juan, J. M., Sanz, J., & Aragón-Àngel, A. (2012). Propagation  
594 of medium scale traveling ionospheric disturbances at different latitudes and solar  
595 cycle conditions. *Radio Science*, 47(06), 1-22.

596 Hines, C. O. (1960), Internal atmospheric gravity waves at ionospheric heights, *Can. J.*  
597 *Phys.*, 38, 1441

598 Horinouchi, T., T. Nakamura, and J. Kosaka (2002), Convectively generated mesoscale  
599 gravity waves simulated throughout the middle atmosphere, *Geophys. Res. Lett.*,  
600 29(21), 2007, doi:10.1029/2002GL016069.

601 Huang, C. Y., Burke, W. H., Machuzak, J. S., Gentile, L. C., & Sultan, P. J. (2002).  
602 Equatorial plasma bubbles observed by DMSP satellites during a full solar cycle:  
603 Toward a global climatology. *Journal of Geophysics*, 107(A12), 1434.

604 Hunsucker RD (1982) Atmospheric gravity waves generated in the high-latitude  
605 ionosphere: a review. *Rev Geophys Space Phys* 20(2):293–315.  
606 doi:10.1029/RG020i002p00293

607 Jonah, O. F., Kherani, E. A., & De Paula, E. R. (2016). Observation of TEC perturbation  
608 associated with medium-scale traveling ionospheric disturbance and possible  
609 seeding mechanism of atmospheric gravity wave at a Brazilian sector. *Journal of*  
610 *Geophysical Research: Space Physics*, 121(3), 2531-2546.

611 Kil, H., Paxton, L. J., & Oh, S.-J. (2009). Global bubble distribution seen from  
612 ROCSAT-1 and its association with the pre-reversal enhancement. *Journal of*  
613 *Geophysical Research*, 114, A06307. doi.org/10.1029/2008JA013672

614 Kotake, N., Y. Otsuka, T. Tsugawa, T. Ogawa, and A. Saito (2006), Climatological study  
615 of GPS total electron content variations caused by medium-scale traveling

616 ionospheric disturbances, *J. Geophys. Res.*, 111, A04306,  
617 doi:10.1029/2005JA011418.

618 Kotake, N., Otsuka, Y., Ogawa, T., Tsugawa, T., & Saito, A. (2007). Statistical study of  
619 medium-scale traveling ionospheric disturbances observed with the GPS networks  
620 in Southern California. *Earth, planets and space*, 59(2), 95-102.

621 Kubota, M., M. Conde, M. Ishii, Y. Murayama, and H. Jin (2011), Characteristics of  
622 nighttime medium-scale traveling ionospheric disturbances observed over Alaska,  
623 *J. Geophys. Res.*, 116, A05307, doi:10.1029/2010JA016212.

624 Lakshmi Narayanan, V., Shiokawa, K., Otsuka, Y., & Saito, S. (2014). Airglow  
625 observations of nighttime medium-scale traveling ionospheric disturbances from  
626 Yonaguni: Statistical characteristics and low-latitude limit. *Journal of Geophysical*  
627 *Research: Space Physics*, 119(11), 9268-9282.

628 Lee, C. C., Y. A. Liou, Y. Otsuka, F. D. Chu, T. K. Yeh, K. Hoshinoo, and K. Matunaga  
629 (2008), Nighttime medium-scale traveling ionospheric disturbances detected by  
630 network GPS receivers in Taiwan, *J. Geophys. Res.*, 113, A12316,  
631 doi:10.1029/2008JA013250.

632 Liu, H. L., McInerney, J. M., Santos, S., Lauritzen, P. H., Taylor, M. A., & Pedatella, N.  
633 M. (2014). Gravity waves simulated by high-resolution whole atmosphere  
634 community climate model. *Geophysical Research Letters*, 41(24), 9106-9112.

635 MacDougall, J., M. A. Abdu, I. Batista, R. Buriti, A. F. Medeiros, P. T. Jayachandran,  
636 and G. Borba (2011), Spaced transmitter measurements of medium scale traveling  
637 ionospheric disturbances near the equator, *Geophys. Res. Lett.*, 38, L16806,  
638 doi:10.1029/2011GL048598.

639 Martinis, C., Baumgardner, J., Mendillo, M., Wroten, J., MacDonald, T., Kosch, M.,  
640 Lazzarin, M., & Umbriaco, G. (2019). First conjugate observations of medium-  
641 scale traveling ionospheric disturbances (MSTIDs) in the Europe-Africa longitude  
642 sector. *Journal of Geophysical Research: Space Physics*, 124, 2213– 2222.  
643 doi.org/10.1029/2018JA026018

644 Mathews, J. D. (1998), Sporadic E: Current views and recent progress, *J. Atmos. Sol.*  
645 *Terr. Phys.*, 60(4), 413–435, doi:10.1016/S1364-6826(97)00043-6.

646 Matsuda, T. S., T. Nakamura, M. K. Ejiri, M. Tsutsumi, and K. Shiokawa (2014), New  
647 statistical analysis of the horizontal phase velocity distribution of gravity waves  
648 observed by airglow imaging, *J. Geophys. Res. Atmos.*, 119, 9707– 9718,  
649 doi:10.1002/2014JD021543.

650 Medvedev, A. V., Ratovsky, K. G., Tolstikov, M. V., Oinats, A. V., Alsatkin, S. S., &  
651 Zherebtsov, G. A. (2017). Relation of internal gravity wave anisotropy with neutral  
652 wind characteristics in the upper atmosphere. *Journal of Geophysical Research:*  
653 *Space Physics*, 122, 7567–7580. doi.org/10.1002/2017JA024103

654 Miller, C. A., W. E. Swartz, M. C. Kelley, M. Mendillo, D. Nottingham, J. Scali, and B.  
655 Reinisch (1997), Electrodynamics of midlatitude spread F : 1. Observations of  
656 unstable, gravity wave-induced ionospheric electric fields at tropical latitudes, J.  
657 Geophys. Res., 102, 11,521–11,532, doi:10.1029/96JA03839.

658 Lakshmi Narayanan, V., Shiokawa, K., Otsuka, Y., & Saito, S. (2014). Airglow  
659 observations of nighttime medium-scale traveling ionospheric disturbances from  
660 Yonaguni: Statistical characteristics and low-latitude limit. Journal of Geophysical  
661 Research: Space Physics, 119(11), 9268-9282.

662 Otsuka, Y., K. Shiokawa, T. Ogawa, and P. Wilkinson (2004), Geomagnetic conjugate  
663 observations of medium-scale traveling ionospheric disturbances at midlatitude  
664 using all-sky airglow imagers, Geophys. Res. Lett., 31, L15803,  
665 doi:10.1029/2004GL020262.

666 Otsuka, Y., Tani, T., Tsugawa, T., Ogawa, T., & Saito, A. (2008). Statistical study of  
667 relationship between medium-scale traveling ionospheric disturbance and  
668 sporadic E layer activities in summer night over Japan. Journal of Atmospheric  
669 and Solar - Terrestrial Physics, 70, 2196–2202.

670 Otsuka, Y., Kotake, N., Shiokawa, K., Ogawa, T., Tsugawa, T., & Saito, A. (2011).  
671 Statistical study of medium-scale traveling ionospheric disturbances observed

672 with a GPS receiver network in Japan. In *Aeronomy of the Earth's Atmosphere and*  
673 *Ionosphere* (pp. 291-299). Springer, Dordrecht.

674 Otsuka, Y., K. Suzuki, S. Nakagawa, M. Nishioka, K. Shiokawa, and T. Tsugawa (2013),  
675 GPS observations of medium-scale traveling ionospheric disturbances over  
676 Europe, *Ann. Geophys.*, 31,163-172,2013, doi:10.5194/angeo-31-163-2013.

677 Paulino, I., de Medeiros, A. F., Buriti, R. A., Takahashi, H., Sobral, J. H. A., & Gobbi,  
678 D. (2011). Plasma bubble zonal drift characteristics observed by airglow images  
679 over Brazilian tropical region Brazilian. *Journal of Geophysics*, 29(2), 239–246.

680 Paulino, I., Medeiros, A. F., Vadas, S. L., Wrasse, C. M., Takahashi, H., Buriti, R. A.,  
681 Leite, D., Filgueira, S., Bageston, J. V., Sobral, J. H. A., and Gobbi, D.: Periodic  
682 waves in the lower thermosphere observed by OI630 nm airglow images, *Ann.*  
683 *Geophys.*, 34, 293–301, <https://doi.org/10.5194/angeo-34-293-2016>, 2016.

684 Perkins, F. (1973), Spread F and ionospheric currents, *J. Geophys. Res.*, 78, 218,  
685 doi:10.1029/JA078i001p00218.

686 Piani, C., D. Durran, M. J. Alexander, and J. R. Holton (2000), A numerical study of  
687 three-dimensional gravity waves triggered by deep tropical convection and their  
688 role in the dynamics of the QBO, *J. Atmos. Sci.*, 57, 3689–3702.

689 Pimenta, A. A., Bittencourt, J. A., Fagundes, P. R., Sahai, Y., Buriti, R. A., Takahashi,  
690 H., & Taylor, M. (2003). Ionospheric plasma bubble zonal drifts over the tropical

691 region: A study using OI 630 nm emission all-sky images. *Journal of Atmospheric*  
692 *Solar Terrestrial Physics*, 65, 1117–1126.

693 Rajesh, P. K., J. Y. Liu, C. H. Lin, A. B. Chen, R. R. Hsu, C. H. Chen, and J. D. Huba  
694 (2016), Space-based imaging of nighttime medium-scale traveling ionospheric  
695 disturbances using FORMOSAT-2/ISUAL 630.0 nm airglow observations, *J.*  
696 *Geophys. Res. Space Physics*, 121, 4769–4781, doi:10.1002/2015JA022334.

697 Resende Chagas, L. C., Arras, C., Batista, I. S., Denardini, C. M., Bertolotto, T. O., &  
698 Moro, J. (2018). Study of sporadic E layers based on GPS radio occultation  
699 measurements and digisonde data over the Brazilian region. In *Annales*  
700 *Geophysicae* (Vol. 36, pp. 587-593).

701 Sahai, Y., Fagundes, P. R., & Bittencourt, J. A. (2000). Transequatorial F-region  
702 ionospheric plasma bubbles: Solar cycle Effects. *Journal of Atmospheric Solar*  
703 *Terrestrial Physics*, 62(15), 1377–1383.

704 Saito, A., T. Iyemori, L. G. Blomberg, M. Yamamoto, and M. Takeda (1998), Conjugate  
705 observations of the mid-latitude electric field fluctuations with the MU radar and  
706 the Freja satellite, *J. Atmos. Sol. Terr. Phys.*, 60, 129–140.

707 Saito, A., M. Nishimura, M. Yamamoto, S. Fukao, T. Tsugawa, Y. Otsuka, S. Miyazaki,  
708 and M. C. Kelley (2002), Observations of traveling ionospheric disturbances and

709 3-m scale irregularities in the nighttime F-region ionosphere with the MU radar  
710 and a GPS network, *Earth Planets Space*, 54, 31–44.

711 Sentman, D. D., E. M. Wescott, R. H. Picard, J. R. Winick, H. C. Stenbaek-Nielsen, E.  
712 M. Dewan, D. R. Moudry, F. T. São Sabbas, M. J. Heavner, and J. Morrill (2003),  
713 Simultaneous observations of mesospheric gravity waves and sprites generated by  
714 a midwestern thunderstorm, *J. Atmos. Terr. Phys.*, 65, 537–550.

715 Sharma, A. K., Nade, D. P., Nikte, S. S., Patil, P. T., Ghodpage, R. N., Vhatkar, R. S.,  
716 Rokade, M. V., & Gurubaran, S. (2014). Occurrence of equatorial plasma bubble  
717 over Kolhapur. *Advances in Space Research*, 54, 435–442.

718 Shiokawa, K., C. Ihara, Y. Otsuka, and T. Ogawa (2003a), Statistical study of nighttime  
719 medium-scale traveling ionospheric disturbances using midlatitude airglow  
720 images, *J. Geophys. Res.*, 108(A1), 1052, doi:10.1029/2002JA009491.

721 Shiokawa, K., Y. Otsuka, C. Ihara, T. Ogawa, and F. J. Rich (2003b), Ground and  
722 satellite observations of nighttime medium-scale traveling ionospheric disturbance  
723 at midlatitude, *J. Geophys. Res.*, 108(A4), 1145, doi:10.1029/2002JA009639.

724 Shiokawa, K., Otsuka, Y., Ogawa, T., and Wilkinson, P.: Time evolution of high-altitude  
725 plasma bubbles imaged at geomagnetic conjugate points, *Ann. Geophys.*, 22,  
726 3137–3143, <https://doi.org/10.5194/angeo-22-3137-2004>, 2004.

727 Shiokawa, K., Y. Otsuka, and T. Ogawa (2006), Quasiperiodic southward moving  
728 waves in 630-nm airglow images in the equatorial thermosphere, *J. Geophys. Res.*,  
729 111, A06301, doi:10.1029/2005JA011406.

730 Sun, L., J. Xu, W. Wang, W. Yuan, Q. Li, and C. Jiang (2016), A statistical analysis of  
731 equatorial plasma bubble structures based on an all-sky airglow imager network  
732 in China, *J. Geophys. Res. Space Physics*, 121, 11,495– 11,517,  
733 doi:10.1002/2016JA022950.

734 Suzuki, S., Shiokawa, K., Otsuka, Y., Ogawa, T., Nakamura, K., & Nakamura, T. (2007).  
735 A concentric gravity wave structure in the mesospheric airglow images. *Journal of*  
736 *Geophysical Research: Atmospheres*, 112(D2).

737 Takeo, K. Shiokawa, H. Fujinami, Y. Otsuka, T. S. Matsuda, M. K. Ejiri, T. Nakamura,  
738 and M. Yamamoto (2017), Sixteen-year variation of horizontal phase velocity and  
739 propagation direction of mesospheric and thermospheric waves in airglow images  
740 at Shigaraki, Japan, *J. Geophys. Res. Spce Physics*, 122, 7849-9088,2017,  
741 doi:10.1002/2017JA023919

742 Tsai, L. C., Su, S. Y., Liu, C. H., Schuh, H., Wickert, J., & Alizadeh, M. M. (2018).  
743 Global morphology of ionospheric sporadic E layer from the FormoSat-  
744 3/COSMIC GPS radio occultation experiment. *GPS Solutions*, 22(4), 118.

745 Tsunoda, R. T. (2006), On the coupling of layer instabilities in the nighttime midlatitude  
746 ionosphere, *J. Geophys. Res.*, 111, A11304, doi:10.1029/2006JA011630.

747 Tsuchiya, S., Shiokawa, K., Fujinami, H., Otsuka, Y., Nakamura, T., Connors, M., ... &  
748 Poddelsky, I. (2019). Three-Dimensional Fourier Analysis of the Phase Velocity  
749 Distributions of Mesospheric and Ionospheric Waves Based on Airglow Images  
750 Collected Over 10 Years: Comparison of Magadan, Russia, and Athabasca, Canada.  
751 *Journal of Geophysical Research: Space Physics*, 124(10), 8110-8124.

752 Tsugawa, T., N. Kotake, Y. Otsuka, and A. Saito (2007a), Medium-scale traveling  
753 ionospheric disturbances observed by GPS receiver network in Japan: A short  
754 review, *GPS Solutions*, 11, 139– 144, doi:10.1007/s10291-006-0045-5.

755 Tsugawa, T., Y. Otsuka, A. J. Coster, and A. Saito (2007b), Medium-scale traveling  
756 ionospheric disturbances detected with dense and wide TEC maps over North  
757 America, *Geophys. Res. Lett.*, 34, L22101, doi:10.1029/2007GL031663.

758 Vadas, S. L., & Fritts, D. C. (2009, January). Reconstruction of the gravity wave field  
759 from convective plumes via ray tracing. In *Annales Geophysicae* (Vol. 27, No. 1,  
760 pp. 147-177). Copernicus GmbH.

761 Vadas, S. L., and G. Crowley (2010), Sources of the traveling ionospheric disturbances  
762 observed by the ionospheric TIDDBIT sounder near Wallops Island on 30 October  
763 2007, *J. Geophys. Res.*, 115, A07324, doi:10.1029/2009JA015053.

764 Whitehead, J. K. (1961), The formation of the sporadic-E layer in the temperate zones,  
765 J. Atmos. Terr. Phys., 20, 49–58, doi:10.1016/0021-9169(61)90097-6

766 Whitehead, J. D. (1989). Recent work on mid-latitude and equatorial sporadic-E.  
767 Journal of Atmospheric and Terrestrial Physics, 51(5), 401-424.

768 Yao, D., & Makela, J. J. (2007). Analysis of equatorial plasma bubble zonal drift  
769 velocities in the pacific sector by imaging techniques. Annales Geophysicae, 25,  
770 701–709.

771 Yeh, W. H., Liu, J. Y., Huang, C. Y., & Chen, S. P. (2014). Explanation of the sporadic-  
772 E layer formation by comparing FORMOSAT-3/COSMIC data with meteor and  
773 wind shear information. Journal of Geophysical Research: Atmospheres, 119(8),  
774 4568-4579.

775 Yokoyama, T., D. L. Hysell, Y. Otsuka, and M. Yamamoto (2009), Three-dimensional  
776 simulation of the coupled Perkins and Es-layer instabilities in the nighttime  
777 midlatitude ionosphere, J. Geophys. Res., 114, A03308,  
778 doi:10.1029/2008JA013789.

779 Yokoyama, T., Shinagawa, H., & Jin, H. (2014). Nonlinear growth, bifurcation, and  
780 pinching of equatorial plasma bubble simulated by three-dimensional high-  
781 resolution bubble model. Journal of Geophysical Research: Space Physics,  
782 119(12), 10-474.

783 Zhou, X., Holton, J. R., & Mullendore, G. L. (2002). Forcing of secondary waves by  
784 breaking of gravity waves in the mesosphere. *Journal of Geophysical Research:*  
785 *Atmospheres*, 107(D7), ACL-3.

786 Zhou, Chen & Tang, Qiong & Song, Xiaoxiao & Qing, Haiyin & Liu, Yi & Wang, Xiang  
787 & Gu, Xudong & Ni, Binbin & Zhao, Zhengyu. (2017). A Statistical Analysis of  
788 Sporadic E layer Occurrence in the Mid-latitude China Region: Sporadic E layer  
789 Occurrence. *Journal of Geophysical Research: Space Physics*. 122.  
790 10.1002/2016JA023135.

791

792

793 **Figure 1**

794 Identification of GPSTEC perturbations over Taiwan. (a) 60 min. high-pass filtered GNSS-TEC for  
795 extracting the MSTID features. (b) Horizontal range of the ionospheric phenomena detection. The  
796 latitude and longitude range are 20-30°N and 115-125°E, respectively, with both zonal and meridional  
797 resolution of ~0.5 degree.

798

799 **Figure 2**

800 Flowchart of the procedure of creating an SVM model for classifying different ionospheric conditions.

801

802 **Figure 3**

803 Local time and seasonal variations of the MSTID obtained from 3D-FFT and SVM analysis over Taiwan  
804 during 2013-2015. It is divided into 10 days and half an hour per grid for calculating the occurrence rate  
805 of southward MSTIDs in (a) 2013 (b) 2014 (c) 2015 year and northward MSTIDs in (d) 2013 (e) 2014  
806 (f) 2015 year. The propagation direction of MSTIDs is compared to the dusk terminator (black line) in  
807 (g) 2013 (h) 2014 (i) 2015 year.

808

809 **Figure 4**

810 Daytime and nighttime MSTID propagation over Japan and Taiwan. (a) An example of typical daytime  
811 MSTIDs over mid- and low-latitude region, and (b) example showing nighttime MSTIDs propagating  
812 from Japan to Taiwan. (c) The filtered TEC perturbations, along the orange dashed line in Figure 4b,  
813 organized as time-distance map.

814

815 **Figure 5**

816 A comparison between propagation direction and normalized PSD of MSTIDs with a dusk terminator  
817 (black line) over Taiwan. The southwestward MSTIDs (deep blue color) in the years (a) 2013 (b) 2014  
818 (c) 2015 is in good agreement with the PSD with greater value (red color) in (d) 2013 (e) 2014 (f) 2015,  
819 suggesting that the southwestward MSTIDs have greater amplitudes than those propagating in other  
820 directions.

821

822 **Figure 6**

823 Comparison of EsL and MSTID occurrence. (a) The occurrence rate of EsL detected by FORMOSAT-  
824 3/COSMIC RO over Taiwan and the conjugate region of Taiwan in nighttime during 2013-2015. (b) The  
825 propagation direction of MSTIDs over Taiwan in nighttime during 2013-2015. (c) The occurrence rate  
826 of southward MSTIDs over Taiwan in nighttime during 2013-2015. (d) The occurrence rate of northward  
827 MSTIDs over Taiwan in nighttime during 2013-2015. The black lines indicate the dusk terminator.

828

829 **Figure 7**

830 The occurrence rate of (a) northwestward, (b) northward and (c) northeastward MSTIDs over Taiwan in  
831 nighttime during 2013-2015. The black lines indicate the dusk terminator.

832

833 **Figure 8**

834 The  $\lambda 557\text{nm}$  airglow images derived from Tainan Astronomical Education Area on 29 April 2020.

835

836 **Figure 9**

837 Two-dimensional filtered GNSS-TEC maps over Taiwan on 29 April 2020.

838

839 **Figure 10**

840 Examples of (a) Zonal Wind and (b) Meridional Wind derived from high-resolution WACCM at  $5.8\text{e-}4$   
841 hpa at 14:00 UT in 9 July. The yellow arrows indicate the propagation direction of the visible AGWs. (c)  
842 Zonal wind and (d) Meridional Wind-time-distance map along the yellow arrow in Figure 10a and 10b,

843 respectively. Each pair of the red symbols indicates an AGWs event. The numbers above the symbols  
844 represent the phase velocity of the AGWs.

845

846 **Figure 11**

847 Comparison between the propagation directions of MSTIDs and the AGWs derived from WACCM. The  
848 gray lines are the MSTID propagation direction during 2013-2015, and the blue line represents the  
849 averaged value during 2013-2015. The red line with stars displays the corresponding WACCM results.

850

# Figures

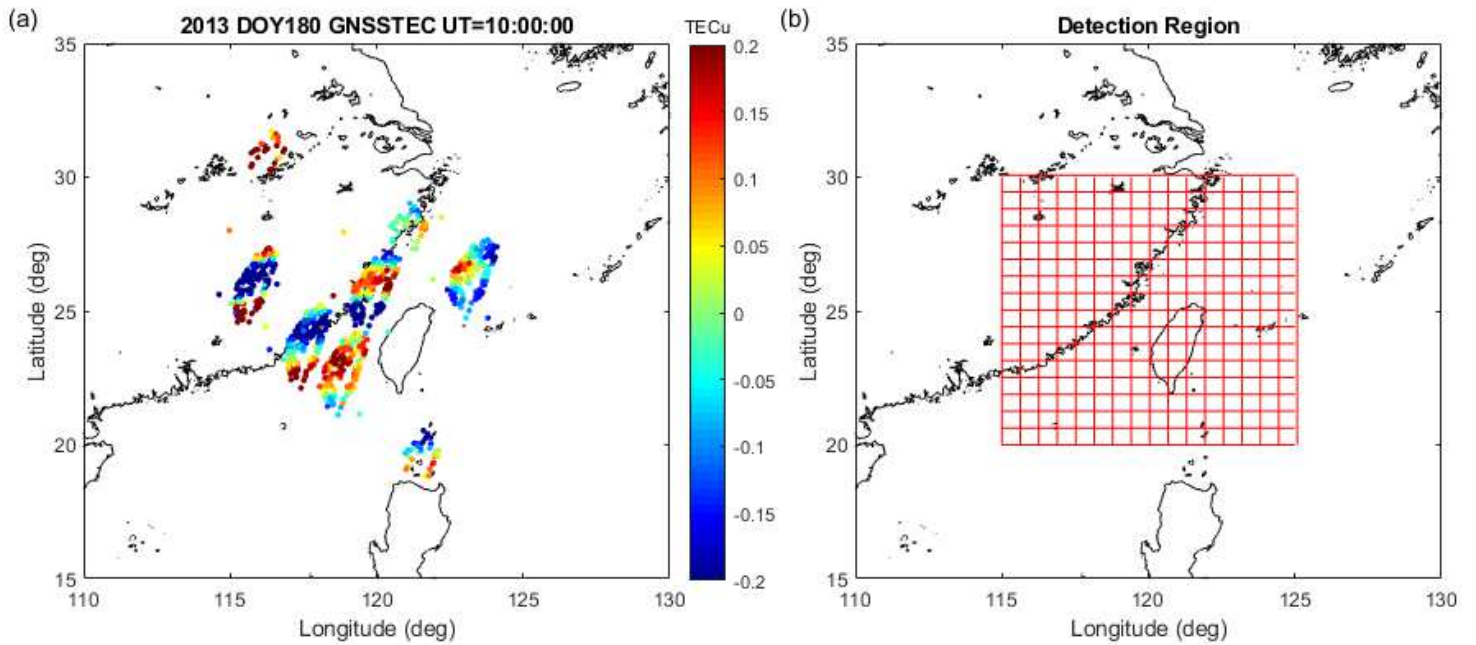


**Figure 1**

Identification of GPSTEC perturbations over Taiwan. (a) 60 min. high-pass filtered GNSS-TEC for extracting the MSTID features. (b) Horizontal range of the ionospheric phenomena detection. The latitude and longitude range are 20-30°N and 115-125°E, respectively, with both zonal and meridional resolution of ~0.5 degree.

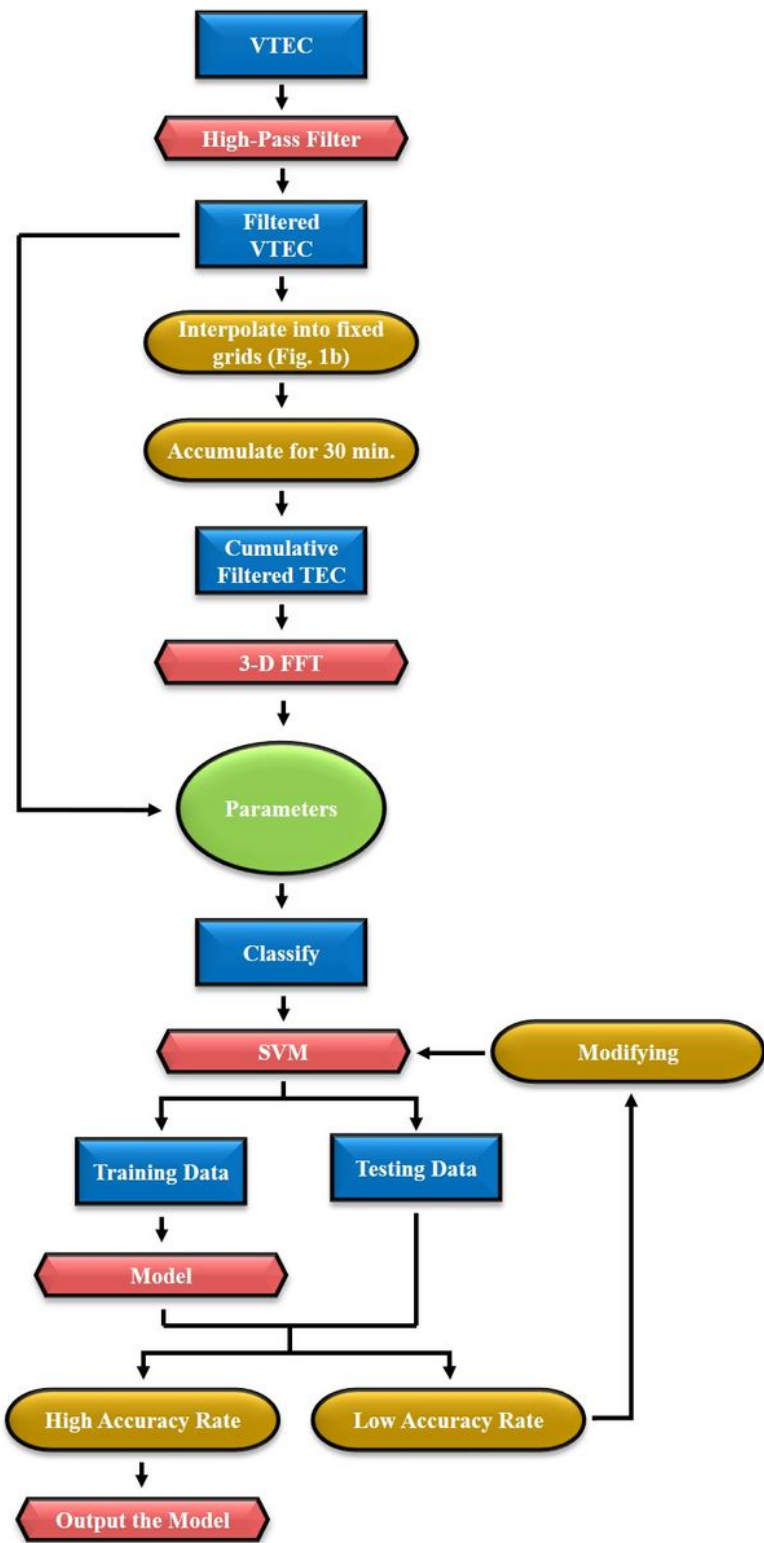
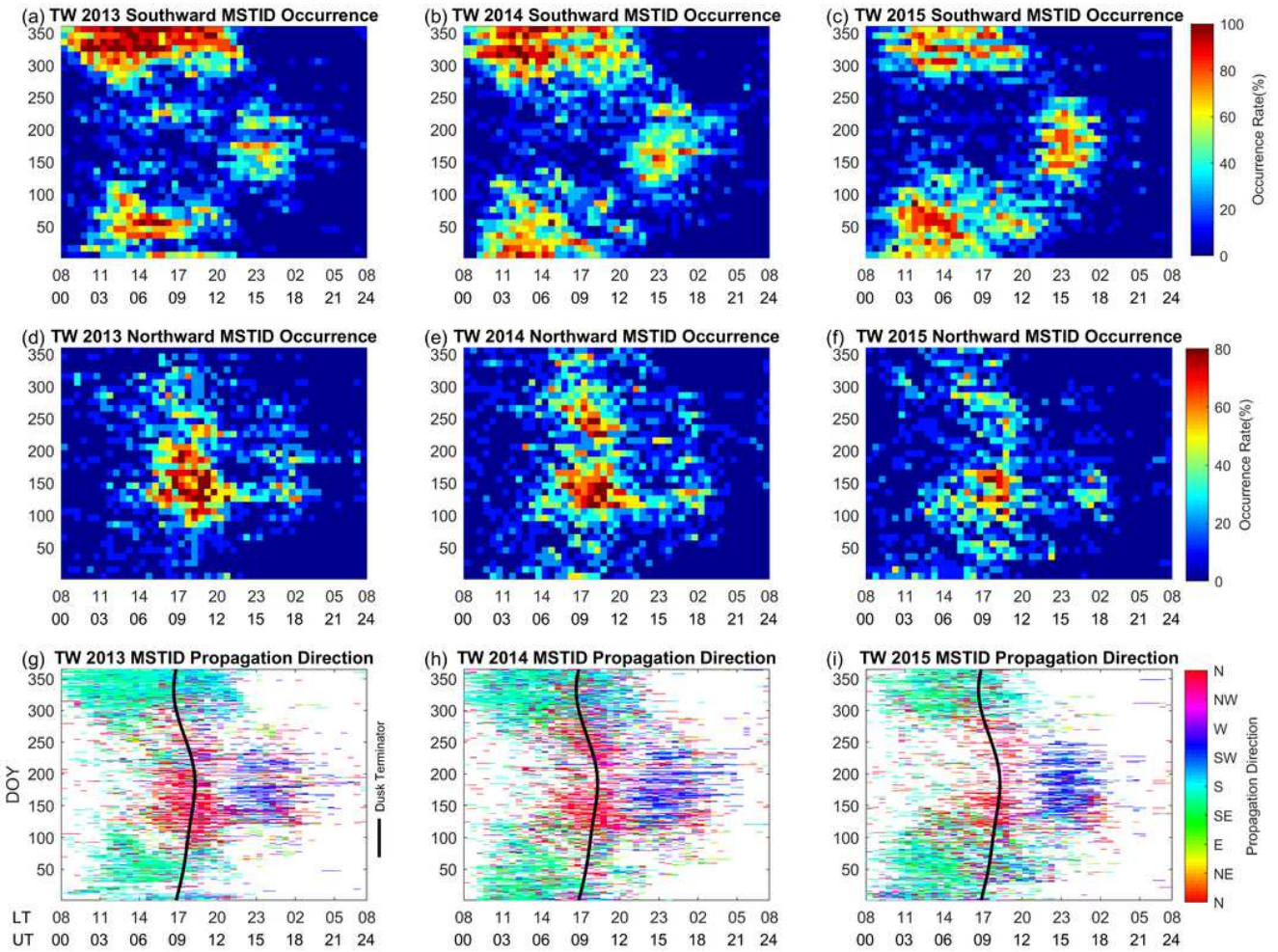


Figure 2

Flowchart of the procedure of creating an SVM model for classifying different ionospheric conditions.



**Figure 3**

Local time and seasonal variations of the MSTID obtained from 3D-FFT and SVM analysis over Taiwan during 2013-2015. It is divided into 10 days and half an hour per grid for calculating the occurrence rate of southward MSTIDs in (a) 2013 (b) 2014 (c) 2015 year and northward MSTIDs in (d) 2013 (e) 2014 (f) 2015 year. The propagation direction of MSTIDs is compared to the dusk terminator (black line) in (g) 2013 (h) 2014 (i) 2015 year.

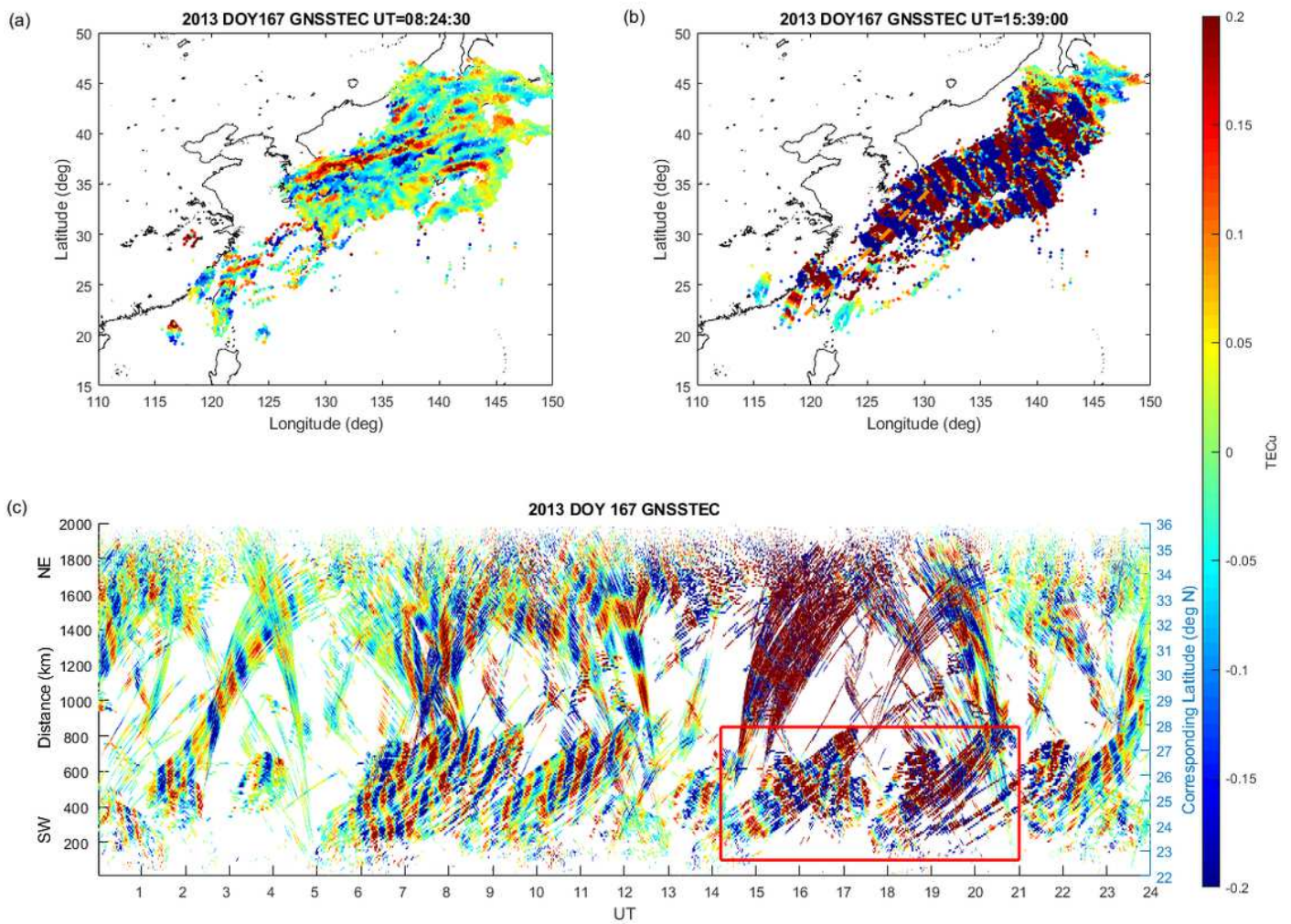


**Figure 4**

Daytime and nighttime MSTID propagation over Japan and Taiwan. (a) An example of typical daytime MSTIDs over mid- and low-latitude region, and (b) example showing nighttime MSTIDs propagating from Japan to Taiwan. (c) The filtered TEC perturbations, along the orange dashed line in Figure 4b, organized as time-distance map.

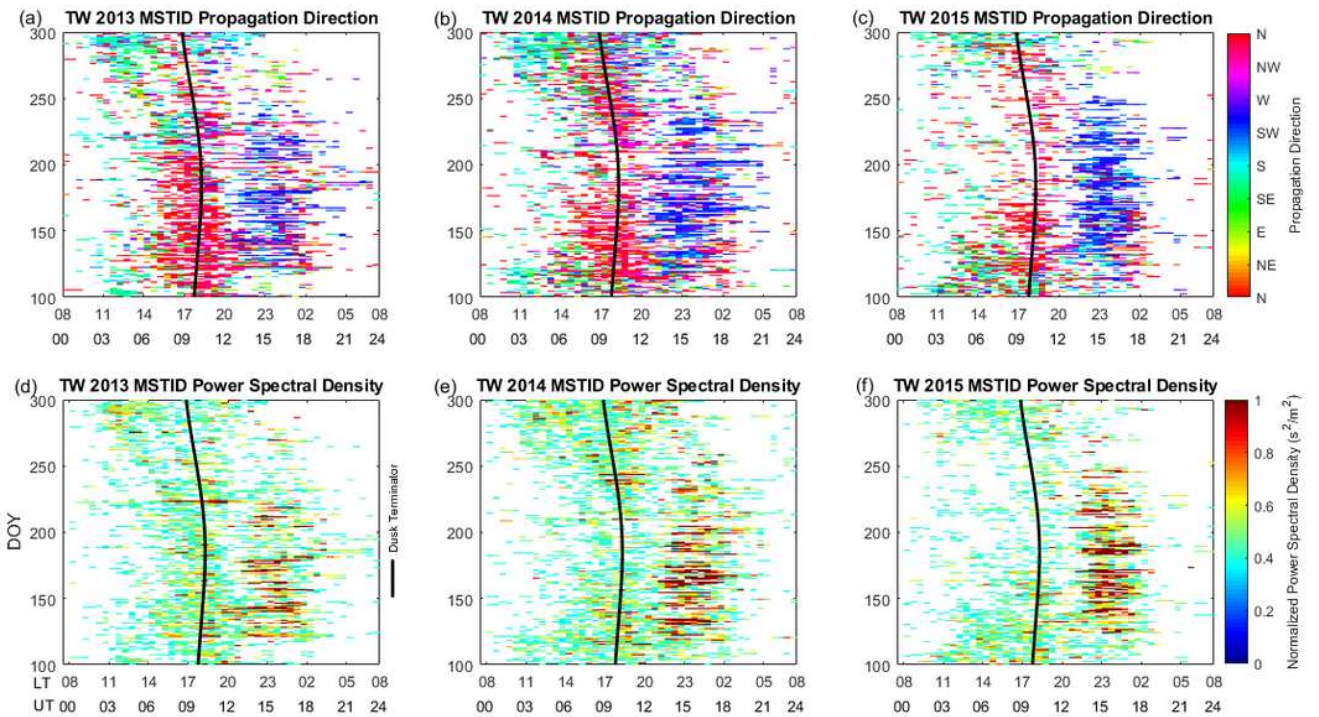


**Figure 5**

A comparison between propagation direction and normalized PSD of MSTIDs with a dusk terminator (black line) over Taiwan. The southwestward MSTIDs (deep blue color) in the years (a) 2013 (b) 2014 (c) 2015 is in good agreement with the PSD with greater value (red color) in (d) 2013 (e) 2014 (f) 2015, suggesting that the southwestward MSTIDs have greater amplitudes than those propagating in other directions.

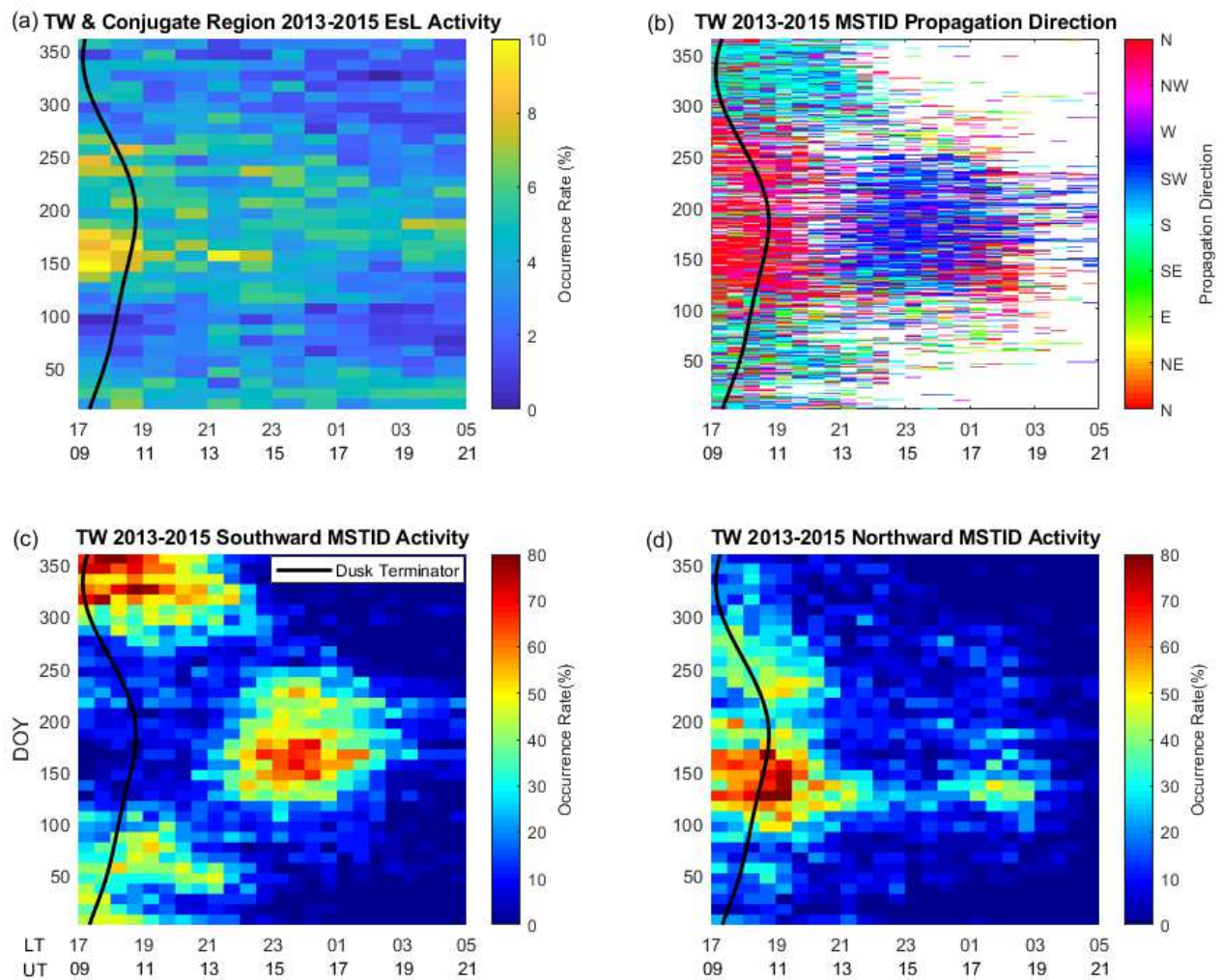


**Figure 6**

Comparison of EsL and MSTID occurrence. (a) The occurrence rate of EsL detected by FORMOSAT-3/COSMIC RO over Taiwan and the conjugate region of Taiwan in nighttime during 2013-2015. (b) The propagation direction of MSTIDs over Taiwan in nighttime during 2013-2015. (c) The occurrence rate of southward MSTIDs over Taiwan in nighttime during 2013-2015. (d) The occurrence rate of northward MSTIDs over Taiwan in nighttime during 2013-2015. The black lines indicate the dusk terminator.

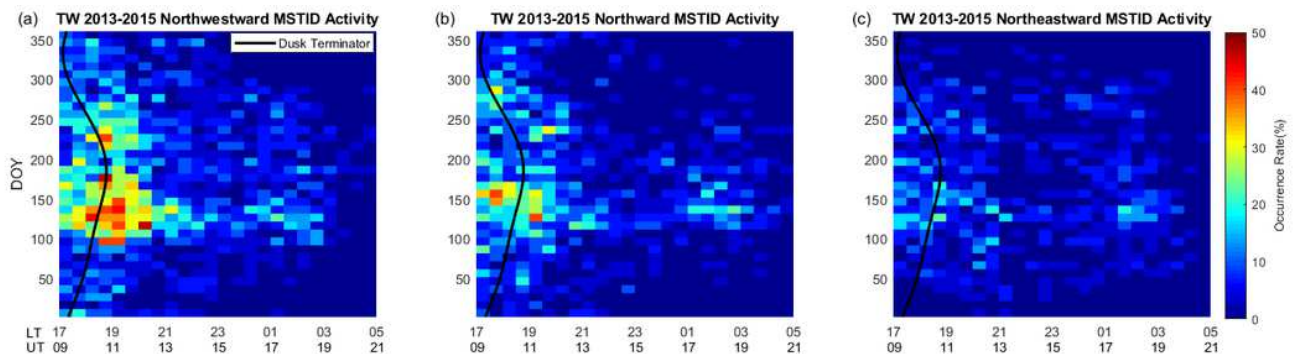


**Figure 7**

The occurrence rate of (a) northwestward, (b) northward and (c) northeastward MSTIDs over Taiwan in nighttime during 2013-2015. The black lines indicate the dusk terminator.

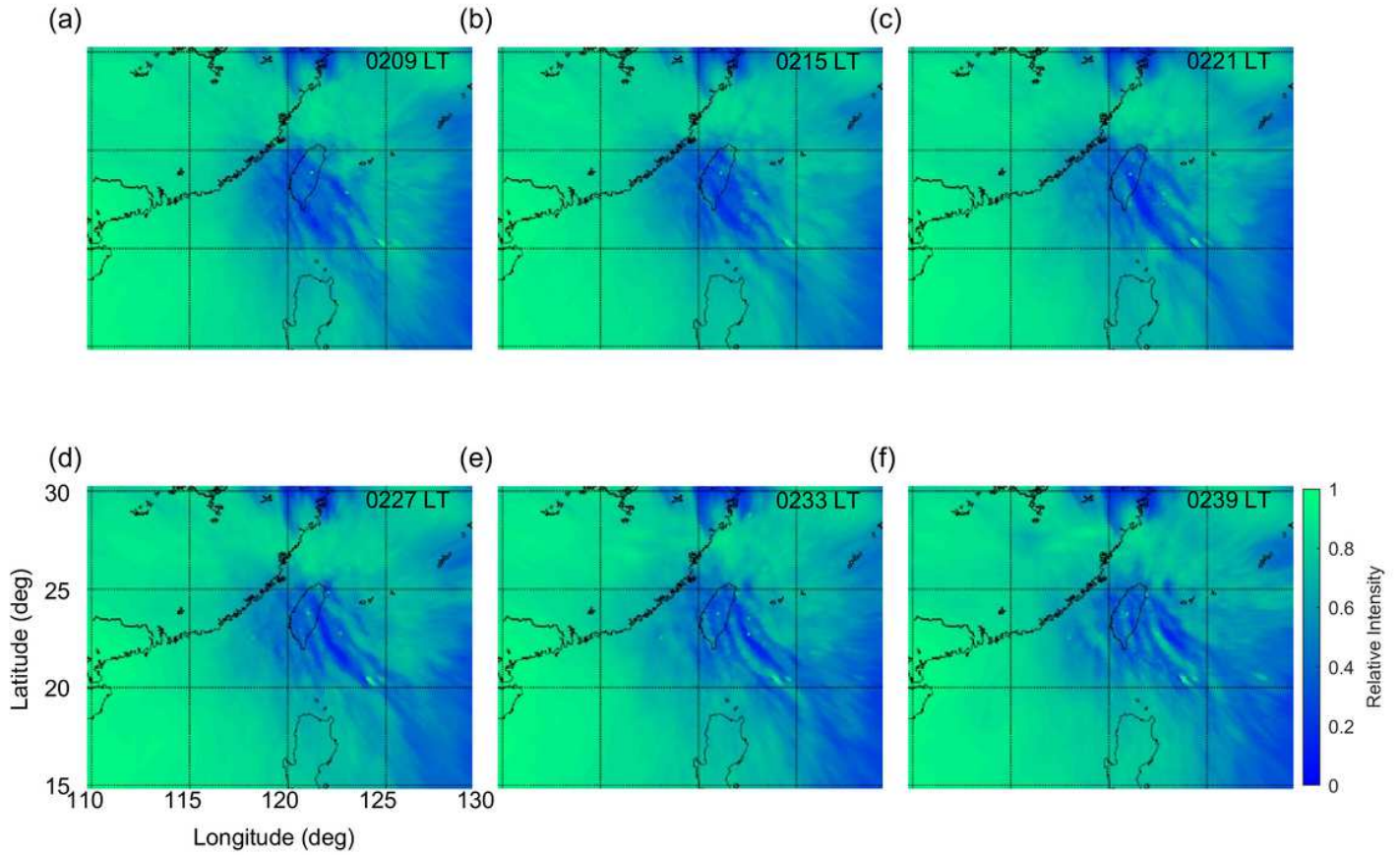
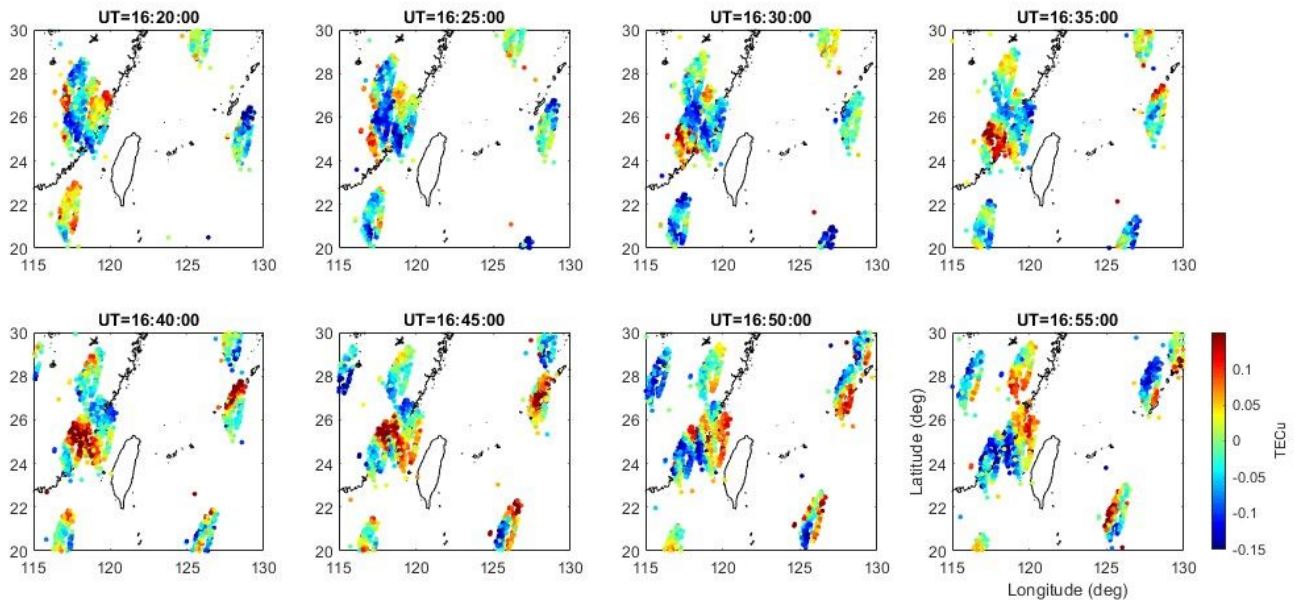


Figure 8

The  $\lambda 557\text{nm}$  airglow images derived from Tainan Astronomical Education Area on 29 April 2020.



**Figure 9**

Two-dimensional filtered GNSS-TEC maps over Taiwan on 29 April 2020.

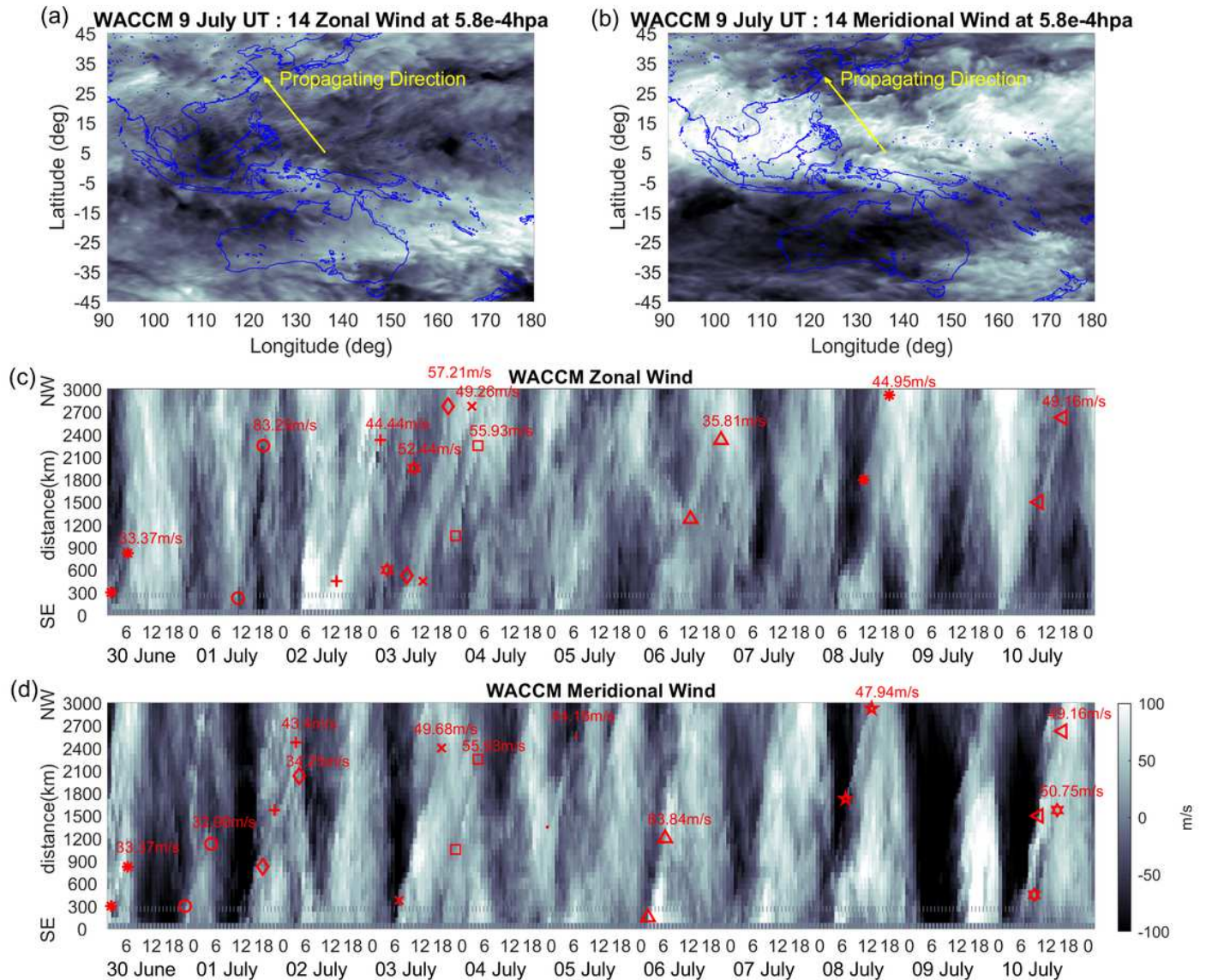


**Figure 10**

Examples of (a) Zonal Wind and (b) Meridional Wind derived from high-resolution WACCM at 5.8e-4 hpa at 14:00 UT in 9 July. The yellow arrows indicate the propagation direction of the visible AGWs. (c) Zonal wind and (d) Meridional Wind-time-distance map along the yellow arrow in Figure 10a and 10b, respectively. Each pair of the red symbols indicates an AGWs event. The numbers above the symbols represent the phase velocity of the AGWs.

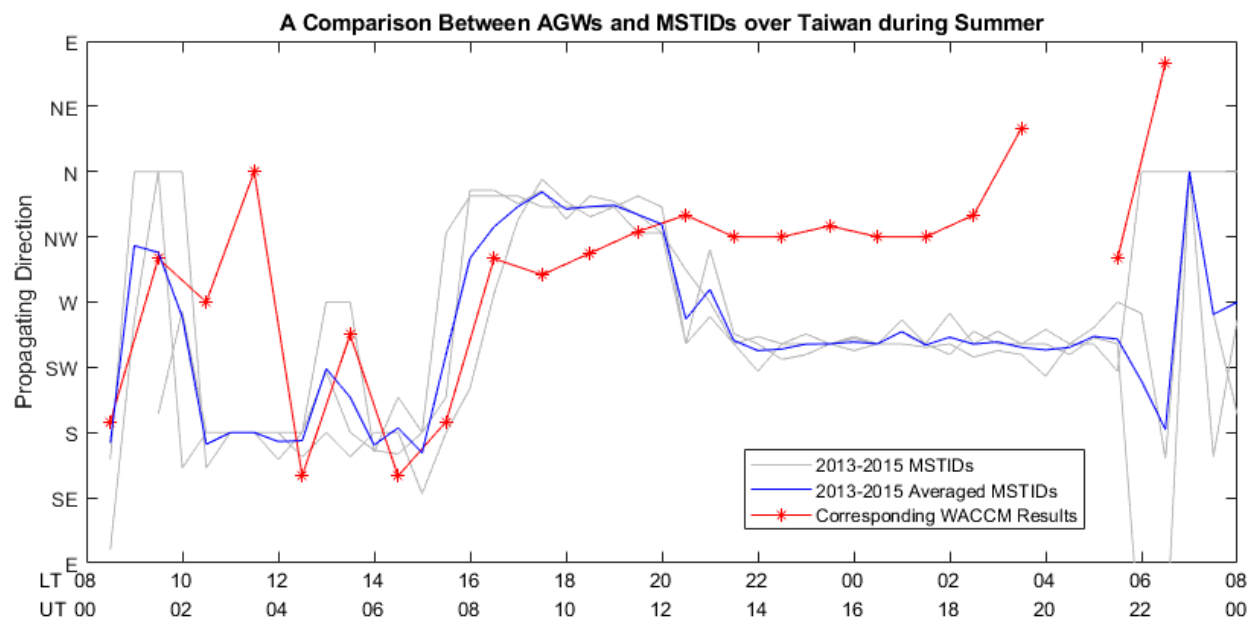


**Figure 11**

Comparison between the propagation directions of MSTIDs and the AGWs derived from WACCM. The gray lines are the MSTID propagation direction during 2013-2015, and the blue line represents the averaged value during 2013-2015. The red line with stars displays the corresponding WACCM results.

## Supplementary Files

This is a list of supplementary files associated with this preprint. Click to download.

- [grapjicalabstract.png](#)